Atmos. Chem. Phys. Discuss., 15, 17797–17842, 2015
www.atmos-chem-phys-discuss.net/15/17797/2015/
doi:10.5194/acpd-15-17797-2015

Atmospheric Chemistry and Physics Discussions

Hygroscopic behavior of NaCl–$MgCl_2$ mixture particles as nascent sea-spray aerosol surrogates and observation of efflorescence during humidifying process

D. Gupta, H.-J. Eom, H.-R. Cho, and C.-U. Ro

Department of Chemistry, Inha University, Incheon, 402-751, Korea

Received: 06 June 2015 – Accepted: 11 June 2015 – Published: 01 July 2015

Correspondence to: C.-U. Ro (curo@inha.ac.kr)

Published by Copernicus Publications on behalf of the European Geosciences Union.

Abstract

NaCl and $MgCl_2$ are the two major constituents of seawater, so NaCl–$MgCl_2$ mixture particles can be a better representative of sea-spray aerosols (SSAs) than pure NaCl. However, there have been very few hygroscopic studies of pure $MgCl_2$ and NaCl–$MgCl_2$ mixture aerosol particles despite the $MgCl_2$ moiety playing a major role in the hygroscopic behavior of nascent SSAs. Laboratory-generated pure $MgCl_2$ and NaCl–$MgCl_2$ mixture aerosol particles with 12 mixing ratios ($0.01 \leq$ mole fraction of NaCl (X_{NaCl}) ≤ 0.9) were examined systematically by optical microscopy, in-situ Raman microspectrometry (RMS), and scanning electron microscopy/energy dispersive X-ray spectrometry (SEM/EDX) elemental X-ray mapping to observe their hygroscopic behavior, derive the experimental phase diagrams, and obtain the chemical micro-structures. Dry-deposited $MgCl_2{\cdot}6H_2O$ particles exhibited a deliquescence relative humidity (DRH) of ~ 33.0 % and an efflorescence RH (ERH) of 10.8–9.1 %, whereas the nebulized pure $MgCl_2$ and $MgCl_2$-dominant particles of $X_{NaCl} = 0.026$ (eutonic) and 0.01 showed single-stage transitions at DRH of ~ 15.9 % and ERH of 10.1–3.2 %. The characteristic OH-stretching Raman signatures indicated the crystallization of $MgCl_2{\cdot}4H_2O$ at low RHs, suggesting that the kinetic barrier to $MgCl_2{\cdot}6H_2O$ crystallization is not overcome in the timescale of the dehydration measurements. The NaCl–$MgCl_2$ mixture particles of $0.05 \leq X_{NaCl} \leq 0.9$ generally showed two-stage deliquescence: first at the mutual DRH (MDRH) of ~ 15.9 %; and second with the complete dissolution of NaCl at the second DRHs depending on the mixing ratios, resulting in a phase diagram composed of three distinct phases. During dehydration, most particles of $0.05 \leq X_{NaCl} \leq 0.9$ exhibited two-stage efflorescence: first, by the homogeneous nucleation of NaCl; and second, at mutual ERH (MERH) of ~ 10.4–2.9 %, by the crystallization of the $MgCl_2{\cdot}4H_2O$ moiety, also resulting in three distinct phases. Interestingly, particles of $X_{NaCl} = 0.1$ and 0.2 frequently showed 3 different types of mutual deliquescence behaviors. The first type exhibited an MDRH at ~ 15.9 %. The second exhibited the first MDRH at ~ 15.9 %, efflorescence to $MgCl_2{\cdot}6H_2O$ (confirmed by in-

ACPD
15, 17797–17842, 2015

situ RMS) at RH of ∼ 16.1–25.0 %, and a second MDRH at ∼ 33.0 %. The third showed an MDRH at ∼ 33.0 %. Some particles of $X_{NaCl} = 0.1$ and 0.2 also exhibited higher MERHs = 15.2–11.9 % and 23.7–15.3 %, respectively, forming $MgCl_2{\cdot}6H_2O$. These observations suggest that the presence of sufficient condensed water and optimally sized crystalline NaCl ($X_{NaCl} = 0.1$ and 0.2) acting as heterogeneous nucleation seeds helps overcome the kinetic barrier, leading to the structural growth and crystallization of $MgCl_2{\cdot}6H_2O$. SEM/EDX elemental X-ray mapping showed that the effloresced NaCl-rich particles contain homogeneously crystallized NaCl in the center, surrounded by $MgCl_2{\cdot}4H_2O$. The observation of an aqueous phase over a wider RH range for NaCl–$MgCl_2$ mixture particles indicates their more probable heterogeneous chemistry compared to pure NaCl particles as a nascent SSA surrogate.

1 Introduction

Sea-salt or sea-spray aerosols (SSAs) are produced from waves through bubble bursting and constitute the second most abundant natural atmospheric aerosols (25–50 % of the aerosol mass) after mineral dust particles (Finlayson-Pitts and Pitts, 2000). A study of the hygroscopic behavior of inorganic aerosol particles, closely simulating the chemical compositions of nascent sea-salts, should provide valuable insights into several important SSA properties: (i) aerodynamic properties, (ii) cloud-droplet nucleation efficiency, (iii) optical properties, and (iv) physicochemical changes through complicated heterogeneous chemical reactions with various atmospheric gas-phase species (Meskhidze et al., 2013; King et al., 2012; Tang et al., 1997; Haywood and Boucher, 2000; ten Brink, 1998; Krueger et al., 2003). For nascent sea-salts, NaCl is the major constituent, followed by $MgCl_2$, and SO_4^{2-}, Ca^{2+}, K^+, etc. (Seinfeld and Pandis, 2006). Because NaCl constitutes ∼ 80 % of sea-salts by mass, it has long been treated as a nascent SSA surrogate, i.e., the hygroscopic behavior of a single-component NaCl aerosol system has been used to parametrize the thermodynamic and optical properties and cloud activation efficiency of nascent ambient SSAs (Tang

ACPD
15, 17797–17842, 2015

et al., 1997; Niedermeier et al., 2008). On the other hand, nascent SSAs can react with gaseous species, such as NO_x and HNO_3/H_2SO_4, within few minutes to hours of their residence in air (ten Brink, 1998; Saul et al., 2006; Liu et al., 2007). Further, these partially or fully reacted SSAs can interact with volatile organic carbons (VOCs), secondary organic aerosols (SOAs), etc. Previous studies have been performed to explore the hygroscopic properties of these aged SSAs. For example, the hygroscopic behavior of laboratory generated aerosol particles of NaCl mixed with dicarboxylic acids (stable water-soluble organics) was reported (Krieger et al., 2012; Ghorai et al., 2014; Ma et al., 2013). In addition, it was demonstrated that both airborne and laboratory-generated SSAs are complicated in their chemical characteristics and mixing states (Wise et al., 2007, 2009; Prather et al., 2013). Therefore, the current understanding of the hygroscopic properties of ambient SSAs is "low" as reported in a recent review by Meskhidze et al. (2013). The contributions from other constituents, such as sea-salt (ss)-SO_4^{2-}, non-sea-salt (nss)-SO_4^{2-}, NO_3^-, and organics cannot be evaluated further unless the hygroscopic behavior of the primary inorganics in nascent SSAs is clearly defined.

$MgCl_2$, the second most abundant constituent of nascent SSAs, plays a key role in heterogeneous atmospheric chemistry as well as chemical fractionation in ambient or laboratory-generated SSAs. For example, the uptake of gaseous HNO_3 was claimed to be faster on the NaCl–$MgCl_2$ mixture particles than on the pure NaCl particles (Saul et al., 2006; Liu et al., 2007); Mg^{2+} and organic species mainly constituted the submicron SSAs generated from a laboratory ocean–atmosphere facility, whereas NaCl dominated the supermicron inorganic SSAs (Prather et al., 2013); in marine aerosols, a Mg^{2+}-rich chloride moiety was segregated from the NaCl moiety (Wise et al., 2007); and the SSAs collected at an Antarctic coastal site (Hara et al., 2012) and during the JASE traverse campaign (Hara et al., 2014) were fractionated into Mg-rich and NaCl-rich salt particles. In addition, it was reported that laboratory-generated SSAs and pure $MgCl_2$ contained residual water, even at very low relative humidity (RH) (Cziczo et al., 1997; Cziczo and Abbatt, 2000; Tang et al., 1997). The hygroscopic growth factors of

ACPD
15, 17797–17842, 2015

ambient or laboratory-generated SSAs plotted as a function of the RH were reported to be different from that of pure NaCl (Tang et al., 1997; Ahn et al., 2010; Schindelholz et al., 2014). This different hygroscopic behavior can affect the cloud droplet nucleation efficiency. For example, the critical supersaturation for the cloud droplet nucleation of particles generated from an artificial seawater–oxalic acid mixture was closer to that of NaCl–$MgCl_2$– oxalic acid mixture particles than that of NaCl–oxalic acid mixture (Drozd et al., 2014). Therefore, NaCl–$MgCl_2$ mixture particles can be a better surrogate for representing the hygroscopic behavior of nascent SSAs.

To obtain a better understanding for hygroscopic behavior of the NaCl–$MgCl_2$ mixture particles, the hygroscopic properties of pure NaCl and $MgCl_2$ salts need to be understood first. The hygroscopic properties of pure NaCl particles are well established. Briefly, during the humidifying process, where RH is changed from low to high, solid NaCl particles at low RH dissolve completely and form aqueous droplets at the deliquescence RH (DRH) of ∼ 75 %. During the dehydration process, where RH is changed from high to low, the concentration of NaCl in the aqueous droplets becomes dense as the RH is decreased and NaCl finally crystallizes at its efflorescence RH (ERH) of ∼ 45–47 %, which is significantly lower than its DRH (Martin, 2000).

However, there have been few hygroscopic studies of pure $MgCl_2$ aerosol particles, even though the $MgCl_2$ moiety plays a major role in the hygroscopic behavior of nascent SSAs. $MgCl_2{\cdot}6H_2O$ is the most thermodynamically stable hydrate of bulk $MgCl_2$ crystals with a DRH of 33 % at room temperature (Lide, 2002). Thus far, only two experiments reported a DRH of ∼ 33 % for aerosol particles nebulized from a $MgCl_2{\cdot}6H_2O$ aqueous solution (Ha and Chan, 1999; Park et al., 2009). On the other hand, in a flow tube FTIR measurement, it was reported that dry $MgCl_2$ particles began to uptake water at RHs $\ll$ 33 %, even though the DRH values were not clearly defined (Cziczo and Abbatt, 2000). Furthermore, just one experiment reported ERH of 14 (±4) % (T = 243 K) for $MgCl_2$ aerosol particles (Gough et al., 2014). Therefore, the hygroscopic behavior of pure $MgCl_2$ aerosol particles was examined systematically in this work for the first time.

ACPD
15, 17797–17842, 2015

To the best of the authors' knowledge, there has been no systematic experimental work on the hygroscopic behavior of binary NaCl–$MgCl_2$ mixture particles. In the only report thus far, for an equimolar mixing ratio of NaCl and $MgCl_2$, Chan et al. (2000) observed the first ERH at 38 % and calculated a mutual DRH (MDRH) of 32 % and a second DRH of 70 % based on the bulk NaCl–$MgCl_2$–H_2O system phase diagram (Seidell and Linke, 1965).

In the present study, the hygroscopic behavior, physical states/phases, and microstructures of pure $MgCl_2$ and NaCl–$MgCl_2$ mixture particles (covering twelve mixing ratios with NaCl mole fractions ranging from 0.01 to 0.9) were examined by optical microscopy (OM), in-situ Raman microspectrometry (RMS) and scanning electron microscopy/energy dispersive X-ray spectrometry (SEM/EDX). The phase transitions of the micrometer sized, laboratory-generated aerosol particles at room temperature were observed by monitoring the size change of the particles in the optical images as a function of the RH. The experimentally measured MDRHs and DRHs were compared with those derived theoretically from the Aerosol Inorganic–Organic Mixtures Functional group Activity Co-efficients (AIOMFAC) model calculations (http://www.aiomfac.caltech.edu) (Zuend et al., 2008, 2011). In-situ RMS was used to observe the phase/structural changes to complement the measurements by OM. SEM/EDX elemental X-ray mapping was used to examine the compositional distribution in effloresced particles. This study systematically describes the full hygroscopic behavior of NaCl–$MgCl_2$ binary aerosol particles at twelve different mixing ratios.

2 Experimental section

2.1 Preparation of NaCl–$MgCl_2$ mixture particles

Mixed NaCl–$MgCl_2$ particles were generated by the nebulization of aqueous solutions with different NaCl : $MgCl_2$ mixing ratios. Pure solutions (1.0 M each) of NaCl and $MgCl_2{\cdot}6H_2O$ (NaCl > 99.9 % purity, Aldrich; $MgCl_2{\cdot}6H_2O$, 99.9 % purity, Aldrich)

ACPD
15, 17797–17842, 2015

were prepared, and solutions with 12 different mixing ratios were made by mixing the two solutions volumetrically. A single jet atomizer (HCT4810) was used to generate the aerosol particles to be deposited on the substrates. For all OM observations and most in-situ RMS measurements, the substrate used was Parafilm-M, which is a hydrophobic substrate with a contact angle of 106.8±0.4° for de-ionized water droplets (Eom et al., 2014). Pure NaCl particles were wet-deposited on the Parafilm-M substrates and their hygroscopic properties were measured to check the accuracy of the experimental set-up. A dry powder or nebulized pure $MgCl_2{\cdot}6H_2O$ particles and some NaCl–$MgCl_2$ mixture particles were deposited on a TEM grid and/or Al substrates to perform off-line SEM/EDX measurements after the hygroscopic measurements by OM to avoid charging by the electron-beam on the Parafilm-M substrates. The size of the dry- and wet-deposited particles ranged from 1 to 10 µm.

NaCl–$MgCl_2$ mixture particles with 12 different mixing ratios were investigated, i.e., 11 compositions with NaCl mole fractions of 0.01–0.9 (X_{NaCl} = 0.01, 0.05, 0.1, 0.2, 0.3, 0.4, 0.5, 0.6, 0.7, 0.8, and 0.9, where X_{NaCl} represents the mole fraction of NaCl.) and a eutonic composition (X_{NaCl} = 0.026, which was calculated from the ionic activity products predicted by the AIOMFAC model). Unlike the eutonic compositions of other binary mixture particles, such as NaCl–KCl (X_{NaCl} = 0.7) (Li et al., 2014) and NaCl–$NaNO_3$ (X_{NaCl} = 0.38) (Gupta et al., 2015), the NaCl–$MgCl_2$ mixture system has a $MgCl_2$-dominant eutonic composition. In the context of thermodynamics, particles with a composition of $X_{NaCl} > 0.026$ were defined as NaCl-rich and those with $X_{NaCl} < 0.026$ were defined as $MgCl_2$-rich.

2.2 Hygroscopic property measurement

2.2.1 Optical microscopy (OM)

The hygroscopic properties of the particles were investigated using a "see-through" inertia impactor apparatus equipped with an optical microscope. The experimental set-up is described in detail elsewhere (Ahn et al., 2010). Briefly, the apparatus was

ACPD
15, 17797–17842, 2015

composed of three parts: (A) see-through impactor, (B) optical microscope, and (C) humidity controlling system. The Parafilm-M substrate onto which the aerosol particles were deposited was mounted on the impaction plate in the see-through impactor. The RH inside the impactor was controlled by mixing dry and wet (saturated with water vapor) N_2 gases. The wet N_2 gas was obtained by bubbling through two deionized water reservoirs. The flow rates of the dry and wet N_2 gases were controlled by mass flow controllers to obtain the desired RH in the range of ~ 3–90 %, which was monitored by a digital hygrometer (Testo 645). The digital hygrometer was calibrated using a dew-point hygrometer (M2 Plus-RH, GE), providing RH readings of ±0.5 % reproducibility. Each humidity condition was sustained for at least 2 min to achieve a steady state for condensing or evaporating water. The particles on the impaction plate were observed through a nozzle throat using an optical microscope (Olympus, BX51M) equipped with 50 × /0.5 numerical aperture objective. The images of particles were recorded by a digital camera (Canon EOS 5D, full frame, Canon EF f/3.5 L macro USM lens) during the humidifying (by increasing RH from ~ 3 to 90 %) and dehydration (by decreasing RH from ~ 90 to 3 %) experiments. The image size was 5616 × 3744 pixels and the image recording condition was set according to the ISO500. The exposure time was 0.4 s and the depth of focus (DOF) was F/3.5. All the hygroscopic experiments were carried out at room temperature ($T = 23 \pm 1\,^{\circ}C$).

The changes in particle size with the variation of RH was monitored by measuring the particle areas in the optical images (Ahn et al., 2010). The particle images were processed using image analysis software (Matrox, Inspector v9.0). The size of the imaging pixel was calibrated using 10 µm Olympus scale bars. Particles larger than 0.5 µm in 2-D diameter (D_p) could be analyzed using this system.

2.2.2 In-situ Raman microspectrometry (RMS)

In-situ RMS measurements were carried out under controlled RHs to observe the structural changes in the hydrated water in $MgCl_2$ crystalline solids. The apparatus is composed of three parts: (a) see-through impactor, (b) Raman microscope/spectrometer,

ACPD
15, 17797–17842, 2015

and (c) humidity controlling system. The experimental set-up is similar to that used for optical microscopy, with the Raman spectrometer replacing the optical microscope, i.e., the particle impaction and RH controlling system are precisely the same as for the standalone optical microscopy system. The RH was monitored using a digital hygrometer (Testo 635). The digital hygrometer was calibrated using a dew-point hygrometer (M2 Plus-RH, GE), providing RH readings with ± 1.5 % reproducibility. The in-situ Raman spectra of the particles deposited on Parafilm-M or Al substrates were recorded using a confocal Raman microspectrometer (XploRA, Horiba Jobin Yvon) equipped with a 50x/0.5 numerical aperture objective (Olympus). The optical image size was 908 × 680 pixels. An excitation laser with a wavelength of 532 nm and 3 mW power was used and the scattered Raman signals were detected using an air cooled multichannel charge-coupled device (CCD) detector. The data acquisition time was 10 s for each measurement. The spectral resolution was 1.8 cm^{-1}. The spectra and images were acquired and processed using Labspec6 software.

OM images have a higher spatial resolution (5616×3744 pixels) than the RMS optical images (908×680 pixels), so that they can be processed more accurately for monitoring the 2-D size changes and the two measurements were performed separately. Unlike the closely monitored OM images, which were recorded in RH steps of ∼ 0.3 % to generate the 2-D area growth curves (Ahn et al., 2010), the Raman spectra of the individual particles were recorded in RH steps of ∼ 3.0 % (∼ 10 min for an ensemble of particles at each RH) to detect the phase changes and complement the OM data.

2.3 SEM/EDX elemental X-ray mapping of effloresced particles

After the hygroscopicity measurements of the individual particles, SEM/EDX was performed on the effloresced NaCl–$MgCl_2$ mixture particles to determine the morphology and spatial distribution of the chemical elements (Li et al., 2014; Gupta et al., 2015). The SEM/EDX measurements were carried out using a Jeol JSM-6390 SEM equipped with an Oxford Link SATW ultrathin window EDX detector. The resolution of the detector was 133 eV for Mn K_α X-rays. The X-ray spectra and elemental X-ray maps were

ACPD
15, 17797–17842, 2015

recorded using Oxford INCA Energy software. A 10 kV accelerating voltage and 0.5 nA beam current was used and the typical measuring times for elemental X-ray mapping were 5 min.

3 Results and discussion

3.1 Hygroscopic behavior of the pure NaCl and $MgCl_2$ particles

Figure 1 shows the 2-D area ratio plots as a function of the RH for the representative wet-deposited NaCl and $MgCl_2$ particles. The humidifying and dehydration curves are represented as the area ratio (A/A_0: left-hand axis), where the 2-D projected particle area at a given RH (A) is divided by that before starting the humidifying process (A_0).

As shown in Fig. 1a, all 26 wet-deposited aerosol particles on an optical image field, which were generated by nebulization from a pure NaCl aqueous solution, showed typical hysteresis curves with DRH of 75.1 (±0.5) % and ERH of 47.6–45.7 %, and these values are consistent with the reported values (Tang et al., 1997; Wise et al., 2007) and previous results (Ahn et al., 2010; Eom et al., 2014).

All 30 wet-deposited aerosol particles nebulized from a 1 M $MgCl_2{\cdot}6H_2O$ aqueous solution showed a prompt deliquescence transition at DRH of 15.9 (±0.3) % and a distinct efflorescence transition in the RH range of 10.1–3.2 % with a mean ERH of 5.9 % (Fig. 1b). At room temperature, thermodynamically stable bulk solids are in the form of $MgCl_2{\cdot}6H_2O$, which was reported to have a DRH of ~ 33.0 % (Lide, 2002). On the other hand, the AIOMFAC model predicts its DRH as 36.7 %, which is somewhat biased on the higher side. Until now, just two experiments reported the DRH as ~ 33.0 %, which is similar to the thermodynamic bulk DRH of $MgCl_2{\cdot}6H_2O$, for aerosol particles nebulized from an $MgCl_2{\cdot}6H_2O$ aqueous solution despite no ERHs being obtained (Ha and Chan, 1999; Park et al., 2009). On the other hand, in a flow tube FTIR measurement, it was reported that the dry $MgCl_2$ particles began to uptake water at much lower RHs than 33 %, which is similar to the current results, even though the DRH values were not de-

ACPD
15, 17797–17842, 2015

fined (Cziczo and Abbatt, 2000). In addition, they suggested the presence of an $MgCl_2$ hydrate crystal at RH of < 2 %. Until now, no ERH for $MgCl_2$ aerosol particles has been reported, with the exception of one at T = 243 K, which was 14 (±4) % (Gough et al., 2014).

As the observation of a distinct DRH and ERH indicated the presence of a crystalline $MgCl_2$ hydrate after efflorescence, in-situ RMS measurements of dry-deposited (powdery) and nebulized $MgCl_2{\cdot}6H_2O$ particles were performed to identify the crystal form of the hydrates. Figure 2 shows optical images and corresponding Raman spectra for a dry-deposited and a nebulized $MgCl_2{\cdot}6H_2O$ particles, which were recorded during the in-situ RMS measurements. During the humidifying process, the irregular-shaped powder particle existed as crystalline $MgCl_2{\cdot}6H_2O$ until RH = 30.6 %, as confirmed by its typical Raman OH stretching signatures (ν(OH) =~ 3350, 3390, and 3510 cm^{-1}) (Fig. 2a) (Musick et al., 1999; Gough et al., 2014). At RH = 34.7 %, the powder particle became a round droplet and the OH vibration signal for free water (ν(OH) =~ 3420 cm^{-1}) was observed, indicating that the deliquescence transition had occurred in the RH range of 30.6–34.7 %, which is typical for $MgCl_2{\cdot}6H_2O$ solids (DRH = 33 %). During the dehydration process (Fig. 2b), the aqueous $MgCl_2$ droplet kept showing a broad free water Raman signal until RH = 15.7 %. At RH = 10.8 %, the optical image indicated a morphological change (despite the particle remaining in a round shape) and new OH vibration signals (ν(OH) =~ 3405 and ~ 3440 cm^{-1}) typical for $MgCl_2{\cdot}4H_2O$ (Gough et al., 2014) was observed, indicating that crystallization had occurred. The particle morphology and Raman signals remained the same when the RH was reduced further to 4.7 %, indicating no change in the crystal structure of the $MgCl_2{\cdot}4H_2O$ particle. When this $MgCl_2{\cdot}4H_2O$ particle was subjected to a second humidifying process (Fig. 2c), the particles underwent a deliquescence transition at RH of 15.0–16.7 %. This experiment suggests that the $MgCl_2{\cdot}6H_2O$ powder particles could not return to their original form once they had been dissolved in the aqueous phase. For a nebulized, wet-deposited $MgCl_2$ aerosol particle, the RMS measurement results, as shown in Fig. 2d and e, indicated that it was crystalline $MgCl_2{\cdot}4H_2O$, when dried

ACPD
15, 17797–17842, 2015

after wet deposition; dissolved at RH = 15.5–16.5 % during the humidifying process (Fig. 2d); and crystallized back to $MgCl_2{\cdot}4H_2O$ at RH = 7.2–6.8 % during the dehydration process (Fig. 2e), which are within the range of phase transition RHs observed by OM. The wet-deposited supermicron (1–10 µm) aqueous $MgCl_2$ droplets crystallized at a lower solvated state ($MgCl_2{\cdot}4H_2O$) when RH was decreased to ∼ 10.1–3.2 % (OM), rather than the stable crystalline $MgCl_2{\cdot}6H_2O$. In the observed ERH range of ∼ 10.1–3.2 %, the H_2O to Mg^{2+} molar ratio, calculated from the AIOMFAC model (at high supersaturation), was in the range of 5.6–4.1, which is less than the 6 required for the hexahydrate, but > 4, supporting the observed crystallization as the tetrahydrate. For bulk crystalline $MgCl_2{\cdot}6H_2O$, Mg^{2+} ions are solvated first as $[Mg(6H_2O)]^{2+}$ in an octahedral structure and Cl^- ions are attached to this hydrate (Casillas-Ituarte et al., 2010; Callahan et al., 2010; Hennings et al., 2013). During the dehydration process of $MgCl_2$ droplets, the rate of the RH change in the measurement time-scale of 2 min for recording each optical image and even 10 min for recording the Raman spectra of an ensemble of particles appears to be insufficient for the thermodynamically predicted but complex crystalline $MgCl_2{\cdot}6H_2O$ structure to take shape. This indicates the presence of a large kinetic barrier and/or diffusional resistance to the hydrate-ion $[Mg(6H_2O)]^{2+}$ mobilization and nucleation required for the structural growth and crystallization of $MgCl_2{\cdot}6H_2O$ with decreasing availability of condensed water. In real ambient conditions, the RH changes can also be abrupt.

The thermodynamic properties for the dissolution of different hydrates in $MgCl_2{\cdot}xH_2O$ (x = 1, 2, 4, 6) at 298 K were reported to have large uncertainties (Wang et al., 1998), even though anhydrous $MgCl_2$ was predicted to have the same DRH as crystalline $MgCl_2{\cdot}6H_2O$ at 298 K (Kelly and Wexler, 2005). On the other hand, a higher free energy (less stable) and thus higher solubility for $MgCl_2{\cdot}4H_2O$ than for $MgCl_2{\cdot}6H_2O$ can explain the current observation of a lower DRH (15.9 (± 0.3) %) for $MgCl_2{\cdot}4H_2O$ than for $MgCl_2{\cdot}6H_2O$ (∼ 33 %).

ACPD
15, 17797–17842, 2015

3.2 Hygroscopic behavior of NaCl–$MgCl_2$ mixture particles

The theoretical aspects of the hygroscopic properties of binary mixture particles are discussed in detail elsewhere (Li et al., 2014; Gupta et al., 2015). In general, for two-component inorganic hygroscopic salt particles, the equilibrium thermodynamics predict two-stage deliquescence and efflorescence transitions. During the humidifying process, the first deliquescence transition is due to dissolution of the eutonic component at a mutual DRH (MDRH), which is independent of the mixing ratios; and the second transition due to the complete dissolution of a residual solid component at a second DRH, which depends on the mixing ratio of the two components (Wexler and Seinfeld, 1991). Similarly, during the dehydration process, aqueous droplets with double salts should show stepwise efflorescence transitions: a component of the aqueous droplets precipitates first at their specific ERH depending on their mixing ratio and the remaining aqueous eutonic component effloresces at their mutual ERH (MERH), which should be independent of the mixing ratios. Therefore, effloresced particles can form a heterogeneous, core – shell crystal structure owing to the stepwise crystallization process (Ge et al., 1996). Thermodynamic models, such as the Extended Atmospheric Inorganics Model (E-AIM) (http://www.aim.env.uea.ac.uk/aim/aim.php) (Tang, 1976; Ansari and Pandis, 1999; Carslaw et al., 1995; Clegg et al., 1998a, b; Wexler and Clegg, 2002) and the AIOMFAC model (http://www.aiomfac.caltech.edu), can be used to predict the MDRH and second DRHs. On the other hand, as efflorescence is a kinetic or rate-driven process depending on many factors, no general theoretical model that covers the efflorescence of single or multi-component aerosol particles is available (Seinfeld and Pandis, 2006; Cohen et al., 1987; Martin, 2000). Moreover, it was observed that the physical state (i.e., amorphous or crystalline and hydrated or anhydrous nature) of salts plays a vital role in water absorption, diffusion, uptake or dissolution, evaporation, solidification, and morphology changes during the humidifying and dehydration processes (Mikhailov et al., 2009). Therefore, the best way to understand the efflo-

ACPD
15, 17797–17842, 2015

rescence behavior of aerosols is through experimental measurements (Seinfeld and Pandis, 2006).

Hygroscopic measurements were performed on 20–40 particles of each mixing ratio of NaCl–$MgCl_2$ using OM. The hygroscopic behavior of the mixture particles could be divided into three categories, (i) NaCl-rich of $X_{NaCl} \geq 0.3$, (ii) NaCl-rich of $X_{NaCl} = 0.05$, 0.1, and 0.2, and (iii) $MgCl_2$-dominant particles of $X_{NaCl} = 0.01$ and 0.026 (the eutonic composition), which is discussed in the following sections.

3.2.1 NaCl-rich particles of $X_{NaCl} \geq 0.3$

During the humidifying process, NaCl–$MgCl_2$ particles with $X_{NaCl} \geq 0.3$ exhibit two stage deliquescence transitions, as is generally expected for binary electrolytic mixture particles. Figure 3 shows the 2-D area ratio plot for the humidifying and dehydration processes as a function of the RH for a NaCl-rich particle of $X_{NaCl} = 0.9$, which is similar to seawater ($X_{NaCl} = 0.89$) (Lide, 2002), together with the optical images shown at the transition points. Initially at RH = 3.1 %, the optical image of the particle clearly shows its angular crystalline nature. During the humidifying process, the particle size remains constant until RH = ~ 14 %, where a slight decrease in size is observed due to water adsorption at the lattice imperfections of the solid salts in the particle and/or structural rearrangement inside the crystal lattice (Mikhailov et al., 2004; Ahn et al., 2010). A first deliquescence transition was observed from RH = 15.1 to 15.8 %, where the particle morphology changed somewhat at RH = 15.1, and the size increased noticeably at RH = 15.8 %. With further increases in RH, the partially aqueous particle gradually grew until RH = ~ 70.0 %, after which a sharp size increase was noted. The optical image at RH = 73.9 % revealed a solid inclusion, which completely dissolved to form a homogeneous droplet, with the second transition completing at RH = 74.1 %. Subsequently, with further increases in RH, the aqueous droplet undergoes continuous hygroscopic growth, as shown for the larger droplet at RH = 84.5 %. The first phase transition at RH = 15.8 %, i.e., MDRH of the NaCl–$MgCl_2$ system, is assigned to the deliquescence of the $MgCl_2$-dominant eutonic solids in the particle. The observed

ACPD
15, 17797–17842, 2015

MDRH deviates from the calculated value of RH = 36.1 % according to the AIOMFAC model; whereas it is comparable to the observed DRH (= 15.9 (± 0.3) %) of crystalline $MgCl_2 \cdot 4H_2O$ for nebulized pure $MgCl_2$. At the MDRH, the particle consists of a mixed phase of liquid droplets (eutonic solution) and a NaCl solid inclusion, which is clearly visible in the optical image of the droplet at RH = 73.9 %, just before the complete dissolution of pure NaCl at the second DRH of 74.1 %. The second DRH is consistent with the DRH of 74.1 % observed for a nascent SSA particle levitated in an electro-dynamic balance (EDB) by Tang et al. (1997).

The other NaCl-rich particles with compositions of $X_{NaCl} \geq 0.3$ (e.g., $X_{NaCl} = 0.5$ in Fig. 4a) also exhibited two-stage phase transitions during the humidifying process: the first transition at MDRH (RH = 15.9 (±0.2) %) due to deliquescence of the eutonic component and the second transition due to complete deliquescence of the particles. In the equimolar mixture particles ($X_{NaCl} = 0.5$, Fig. 4a), the observed second DRH of 67.6 % (on average, 67.3 (±0.4) %, in terms of reproducibility when the humidifying and dehydration processes were repeated) is consistent with the theoretical DRH of 67.5 % calculated using the AIOMFAC model. For an equimolar mixing ratio, Chan et. al. (2000) estimated a MDRH of 32.0 % and a second DRH of 70 % from the phase diagram of the bulk $NaCl–MgCl_2–H_2O$ system. For the NaCl-rich particles with compositions of $X_{NaCl} \geq 0.3$, the MDRH is independent of the compositions. On the other hand, the second DRHs were dependent on the compositions and shift toward a pure NaCl limit (DRH = 75.1 (±0.5) %) with increasing NaCl mole fraction, as observed for $NaCl–KCl$ and $NaCl–NaNO_3$ mixture particles (Li et al., 2014; Gupta et al., 2015).

During the dehydration process, the representative NaCl-rich particle of $X_{NaCl} = 0.9$ (Fig. 3) showed a two-stage phase transition. The liquid droplet decreased gradually in size with decreasing RH and became supersaturated with respect to NaCl below RH of 74.1 % (DRH for $X_{NaCl} = 0.9$), where the droplet still appeared to be homogeneous (as shown in the optical image at RH = 71.2 %). With the further decreases in RH, the droplet size decreased abruptly at RH = 45.9–45.6 % due to the crystallization of NaCl in the droplet. At RH = 45.6 %, the first ERH for $X_{NaCl} = 0.9$, the particle was composed

ACPD
15, 17797–17842, 2015

of a mixed phase of the eutonic solution and NaCl solids, as observed clearly from the crystal segments in the optical image. With further decreases in RH, the mixed phase droplet shrank gradually until RH = 5.3–5.1 %, where the $MgCl_2$-dominant eutonic component in the particle crystallized. At RH = 5.1 % (MERH), a completely effloresced solid particle was formed, which is clearly seen by the reappearance of an overall angular shape and a bright crystalline segment in the optical image (similar to that at RH = 3.1 %, at the start of the humidifying process). The measured first ERH and MERH for the particles with a composition of X_{NaCl} = 0.9 vary among the particles, 1–10 µm size, in the same optical image field and are in the range, RH = 48.2–45.4 % and RH = 5.6–5.0 %, respectively.

During the dehydration process, the other NaCl-rich particles with compositions of $X_{NaCl} \geq 0.3$ also exhibited two-stage phase transitions. For example, for a particle with X_{NaCl} = 0.5 (Fig. 4a), the first transition due to the efflorescence of pure NaCl occurs at RH = 35.5–35.0 % and the second due to the efflorescence of the eutonic component at RH = 5.7–5.5 %. Chan et al. (2000) reported the first ERH of 38 % (within the range of the first ERHs of 40.5–35.0 % observed in this study for 38 particles), but no MERH (in this work, it was observed in the RH range of 6.9–5.0 %), when they performed the dehydration experiments on a single levitated aqueous droplet of NaCl–$MgCl_2$ with an equimolar mixing ratio (X_{NaCl} = 0.5) in an EDB. The first ERHs for the NaCl-rich mixture particles with compositions of $X_{NaCl} \geq 0.3$ are dependent on the compositions and shift toward the pure NaCl limit (ERH = 47.6–45.7 %) with increasing NaCl mole fraction, as observed for NaCl–KCl and NaCl–$NaNO_3$ mixture particles (Li et al., 2014; Gupta et al., 2015); whereas the MERH, like their MDRH, is almost independent of the particle compositions. The MERHs, however, were observed over a wide RH range (RH = 10.4–2.9 %) due to the stochastic nature of nucleation leading to efflorescence.

3.2.2 NaCl-rich particles of X_{NaCl} = 0.05, 0.1, and 0.2

In the case of NaCl-rich particles with compositions of X_{NaCl} = 0.1 and 0.2, three types of particles showing 2- or 3-stage deliquescence transitions were observed. Figure 5a–

ACPD
15, 17797–17842, 2015

c show the hygroscopic behavior of representative "Types A, B, and C" particles, respectively, where their particle/droplet optical images are also shown at each transition point. During the humidifying process, a Type A particle of $X_{NaCl} = 0.2$ (Fig. 5a) showed an initial small decrease in size due to structural rearrangement before the first deliquescence transition at RH = 15.5–15.8 %. At its MDRH of 15.8 %, bright solids in the particle disappeared due to dissolution of the eutonic component. With further increases in RH, it gradually grew until RH = 56.7 %, after which an abrupt increase in size was observed with the dissolution of pure NaCl, i.e., the second deliquescence transition completing at RH of 57.0 % (resulting in a homogeneous droplet in the optical image).

For Type B particles, three deliquescence and one intermediate efflorescence transitions were observed during the humidifying process (e.g., Fig. 5b). Figure 5b shows that the particle size remained constant until RH = ~ 15.5 %, and then underwent an abrupt first mutual deliquescence transition at RH of 15.5–15.8 % (called $MDRH_1$). The particle grew gradually until the RH reached 21.9 %. Subsequently, an efflorescence-like transition with a decrease in size and a bright, crystallized solid particle were observed at RHs of 21.9–24.9 and 24.9 %, respectively. Thereafter, the size of the Type B particle remained almost constant until RH = 31.0 %, which was followed by a small decrease in size (structural rearrangement) at RH = 32.0 % and then by a second mutual deliquescence transition at RH = 32.3–33.0 % ($MDRH_2$). The observed $MDRH_2$ of 33.0 % for the Type B particle is attributed to the complete dissolution of the crystalline $MgCl_2{\cdot}6H_2O$-dominant eutonic part. With further increases in RH, the size of the Type B particle increased gradually until the third deliquescence transition with the dissolution of pure NaCl (NaCl solid inclusion in the optical image at RH = 56.7 % disappears in the optical image at RH = 57.0 %), which occurs at RH of 56.7–57.0 %, similar to the Type A particle (Fig. 5a). The Type C particle (Fig. 5c) did not show the first deliquescence transition at RH of ~ 15.8 % (seen in Fig. 5a and b) or recrystallization (seen in Fig. 5b), but its size remained unchanged until RH = 31.0 %, followed by a small decrease in size due to the structural rearrangement at RH = 32.0 %, and a sharp increase in size from

ACPD
15, 17797–17842, 2015

RH = 32.3–33.0 %, which is the first deliquescence transition or MDRH. The second deliquescence transition was observed as usual at RH = 56.7–57.0 %.

During the dehydration process, the NaCl-rich particles of $X_{NaCl} = 0.2$ of Types A–C particles showed two-stage phase transitions (Fig. 5a–c). The liquid droplets decreased gradually in size with decreasing RH and became supersaturated with NaCl below RH = 57.0 % (DRH for $X_{NaCl} = 0.2$). With further decreases in RH, the droplet sizes decreased noticeably at RH = 24.1–23.9 % (Fig. 5a), 25.1–24.9 % (Fig. 5b), and 24.9–23.9 % (Fig. 5c), due to the crystallization of NaCl. At the first ERHs of 23.9, 24.9, and 23.9 %, the partially aqueous Types A–C particles, respectively, are composed of a mixed phase of a eutonic solution and NaCl solid. With further decreases in RH, Types A and B droplets gradually shrank until the final perceptible decreases in sizes were observed at RH = 6.1–5.2 % (Fig. 5a) and at RH = 5.4–5.2 % (Fig. 5b), where completely effloresced Types A and B solid particles, respectively, were formed. Their low MERH of 5.2 % suggests that the $MgCl_2{\cdot}4H_2O$-dominant eutonic component was crystallized for the Types A and B particles. For the Type C particle, complete efflorescence occured at RH = 23.9–23.7 % with a MERH of 23.7 % (Fig. 5c). The high MERH suggests that the $MgCl_2$-dominant eutonic part crystallized heterogeneously as the $MgCl_2{\cdot}6H_2O$ moiety on crystalline NaCl seeds, leading to the observed MDRH of ~ 33.0 % for the Type C particle.

To clearly explain the above observations, particles with a composition of $X_{NaCl} = 0.2$ sitting on a Parafilm-M substrate were examined using in-situ RMS. Figure 6 shows the Raman spectra and corresponding optical images, which were recorded during the in-situ RMS measurements of particles of $X_{NaCl} = 0.2$. As shown in Fig. 6a, at RH = 4.5 %, the Type A particle appears irregular and shows a typical –OH stretching signature for crystalline $MgCl_2{\cdot}4H_2O$. At RH = 16.6 %, the Type A particle becomes round-shaped and the broad –OH stretching peak for free-water indicates that it is deliquesced. During the dehydration process, as shown in Fig. 6b, the Type A round droplet at RH = 10.7 becomes irregular-shaped, i.e., effloresces at RH = 7.6 %, forming a crystalline $MgCl_2{\cdot}4H_2O$-dominant eutonic phase. For Type A particles, the NaCl and

ACPD
15, 17797–17842, 2015

$MgCl_2 \cdot 4H_2O$-dominant eutonic solids are dissolved and formed during the humidifying and dehydration processes.

As shown in Fig. 6c, during the humidifying process, the Type B particle appears irregular at low RH (= 4.6 %) and shows a –OH stretching signature for crystalline $MgCl_2 \cdot 4H_2O$. At RH = 16.4 %, the particle becomes round and the broad –OH stretching signal for free water indicates that it is deliquesced. With a small increase in RH (to ~ 16.6 %), however, the Type B particle changes its morphology and shows the typical –OH vibration signatures for crystalline $MgCl_2 \cdot 6H_2O$, indicating the occurrence of efflorescence. At RH = 33.9 %, the Type B particle appears round and shows a free water –OH peak again, indicating that further deliquescence occurs below RH = 33.9 %. During the dehydration process, as shown in Fig. 6d, the Type B round droplet at RH = 15.3 % becomes irregular-shaped, i.e., effloresces at RH = 10.1 %, forming a crystalline $MgCl_2 \cdot 4H_2O$-dominant eutonic phase. For Type B particles, NaCl and $MgCl_2 \cdot 4H_2O$-dominant eutonic solids are formed during the dehydration process, and despite the $MgCl_2 \cdot 4H_2O$-dominant eutonic solids being dissolved, the $MgCl_2 \cdot 6H_2O$-dominant eutonic solids are formed through efflorescence and are dissolved, and finally, the NaCl solids deliquesce during the humidifying process. The efflorescence of the laboratory-generated particles during the humidifying process has never been reported until now.

As shown in Fig. 6f, at RH = 4.5 %, a Type C particle appears irregular and crystalline and shows the typical –OH stretching signature for crystalline $MgCl_2 \cdot 6H_2O$. At RH = 34.1 %, the Type C particle appears round and shows a free water –OH peak, indicating that deliquescence occurs below RH = 34.1 %. As shown in Fig. 6e, the Type C particle effloresces at a considerably high ERH of 16.8 % and shows a typical –OH stretching signature for crystalline $MgCl_2 \cdot 6H_2O$. For the Type C particles, NaCl and $MgCl_2 \cdot 6H_2O$-containing crystals are formed and dissolved during the dehydration and humidifying processes, as clearly confirmed by the OM and in-situ RMS measurements. On the other hand, this Type C particle does not form $MgCl_2 \cdot 6H_2O$ again at the next dehydration process, as shown in Fig. 6g, indicating that this particle is no longer

ACPD
15, 17797–17842, 2015

Type C and the different types of particles are formed somewhat randomly because efflorescence is a kinetic or rate-driven process depending on many factors.

Table 1 shows the encountering frequencies of Types A-C particles at various NaCl-$MgCl_2$ mixing ratios in their respective OM experiments. For all mixing ratios except $X_{NaCl} = 0.1$ and 0.2, Type A particles, which form a crystalline $MgCl_2{\cdot}4H_2O$-dominant eutonic phase at MERH, are dominant. Owing to the decreasing availability of condensed water during dehydration, large kinetic barrier and/or diffusional resistance for hydrate-ion nucleation make the formation of the crystalline $MgCl_2{\cdot}6H_2O$ structure difficult, which is already discussed for the nebulized pure $MgCl_2$ aerosols.

For particles of $X_{NaCl} = 0.1$ and 0.2, the encountering frequencies of Type B particles are 29 and 45 %, respectively, and Type C are 47 and 18 %, respectively, indicating that the formation of $MgCl_2{\cdot}6H_2O$-containing crystals is easier at these mixing ratios. Aqueous moieties in particles were reported to effloresce more easily by heterogeneous nucleation in the presence of seeds (Schlenker and Martin, 2005; Li et al., 2014; Gupta et al., 2015). For Type C particles, the crystallization of $MgCl_2{\cdot}6H_2O$ takes place at a considerably high ERH range of 23.7–11.9 % during dehydration (e.g., see Fig. 5c), suggesting that the NaCl crystals of an optimal size ($X_{NaCl} = 0.1$ and 0.2) can act as seeds for the heterogeneous nucleation of $MgCl_2{\cdot}6H_2O$. On the other hand, this heterogeneous efflorescence of $MgCl_2{\cdot}6H_2O$ is also observed during the humidifying process for Type B particles (Fig. 5b). Efflorescence during the humidifying process was once reported for Amazonian rain-forest aerosols (Pöhlker et al., 2014), where it was claimed that the impacted ambient organic–inorganic mixed aerosols initially had amorphous or poly-crystalline structures and underwent restructuring through kinetic water and ion mobilization, resulting in the crystallization of inorganic salts during hydration. During the humidifying process, the $MgCl_2{\cdot}4H_2O$-dominant eutonic solids in the effloresced Type B particles of $X_{NaCl} = 0.1$ and 0.2 dissolve at $MDRH_1$ (= 15.9 (±0.3) %) and some moisture is also adsorbed on the surface of the crystalline NaCl moiety. The $[Mg(6H_2O)]^{2+}$ hydrate-ions appear to be mobilized in the presence of sufficient condensed water at the observed ERH range of ∼ 16.1–24.9 % during hydration (∼ 23.7–

ACPD
15, 17797–17842, 2015

11.9 % during dehydration) and the kinetic barrier is overcome by heterogeneous nucleation on the optimally-sized NaCl seeds, leading to structural growth and crystallization of the $MgCl_2{\cdot}6H_2O$ moiety. Therefore, particles of $X_{NaCl} = 0.1$ and 0.2 frequently show a characteristic MDRH of ~ 33.0 (±0.5) % for the dissolution of the $MgCl_2{\cdot}6H_2O$-dominant eutonic solids. On the other hand, the crystalline NaCl seeds for the particles of $X_{NaCl} \geq 0.3$, being larger than the optimal size, appear to inhibit the smooth diffusion of water kinetically, which is a primary requirement for the nucleation of $[Mg(6H_2O)]^{2+}$. Therefore, for particles of $X_{NaCl} \geq 0.3$, crystalline $MgCl_2{\cdot}6H_2O$ is not formed in the time scale of the measurements.

In the case of particles of $X_{NaCl} = 0.05$, two-stage deliquescence transitions for Type A particles were mainly observed: mutual deliquescence occurring at MDRH of 16.0 (±0.3) % and the second DRH for the remnant NaCl at RH of 40.5 (±1.5) %. The frequency to encounter Types B and C particles for $X_{NaCl} = 0.05$ was much less (Table 1), probably because the NaCl seeds were smaller than the optimal size.

For the NaCl-rich particles of $X_{NaCl} = 0.05$, 0.1, and 0.2, the second DRHs were dependent on the compositions and shifted toward the pure NaCl limit (DRH = 75.1 (±0.5) %) with increasing NaCl mole fraction. Figure 7 plots the measured DRHs for the NaCl-rich particles with various compositions as a function of the NaCl mole fraction, showing that the experimental second DRH values are in good agreement with the values calculated from the AIOMFAC model. On the other hand, the observed MDRH (= 15.9 (±0.3) %) for Type A particles deviates from that predicted by the thermodynamic considerations in the model. In contrast, the observed $MDRH_2$ for the Type B particles and MDRH for the Type C particle of 33.0 (±0.5) % agree with the predicted DRH for $MgCl_2{\cdot}6H_2O$.

In the case of $X_{NaCl} = 0.2$, the measured first ERH and MERH vary among Types A and B particles, 1–10 µm in size, on the same optical image field and are in the range of RH = 27.1– 23.9 % (average first ERH = 25.0 %) and RH = 10.2–5.2 % (average MERH = 7.1 %), respectively. In contrast, the Type C particles exhibit MERH in the range of 23.7–15.3 % (average MERH = 18.1 %). For Types A and B particles of

ACPD
15, 17797–17842, 2015

X_{NaCl} = 0.1, the measured first ERH and MERH vary in the range of RH = 17.4–12.4 % (average first ERH = 15.8 %) and RH = 9.4–6.5 % (average MERH = 7.2 %), respectively, whereas Type C particles exhibit MERH in the range of 15.2–11.9 % (average MERH = 13.3 %). In the case of X_{NaCl} = 0.05, the measured first ERH and MERH vary in the range of RH = 15.5–13.0 % (average first ERH = 13.2 %) and RH = 9.3–6.5 % (average MERH = 6.9 %), respectively. Figure 8 shows the measured ERHs for the NaCl-rich particles with various compositions as a function of the NaCl mole fraction.

3.2.3 $MgCl_2$-dominant particles of X_{NaCl} = 0.01 and 0.026 (the eutonic composition)

Figure 4b and c presents the 2-D area ratio plots for the $MgCl_2$-dominant particles with the eutonic composition (X_{NaCl} = 0.026) and of X_{NaCl} = 0.01 as a function of RH. During the humidifying process, the particles of X_{NaCl} = 0.026 and 0.01 show single-stage deliquescence phase transitions from RH = 15.7 to 16.1 % and from RH = 15.6 to 16.1 %, respectively. With further increases in RH, the particles showed continuous and gradual hygroscopic growth. During the dehydration process, the particles of X_{NaCl} = 0.026 and 0.01 decreased gradually in size until they exhibited hysteresis with single-stage efflorescence transitions from RH = 5.3 to 4.5 % and from RH = 4.8 to 4.6 %, respectively. Therefore, the hygroscopic behavior of these particles with $MgCl_2$-dominant compositions is similar to that of the nebulized pure $MgCl_2$ particles (Fig. 1b).

The probability of forming a crystalline $MgCl_2{\cdot}6H_2O$ structure for particles of X_{NaCl} = 0.026 and 0.01 is quite low (Table 1), due to the low probability of heterogeneous nucleation in the absence of optimally-sized seeds, as explained above for the case of X_{NaCl} = 0.05. NaCl, which is mostly in the aqueous phase, cannot act as a crystalline seeds for heterogeneous nucleation at low RHs, or the sizes of those NaCl seeds are too small for heterogeneous nucleation leading to the formation of a hexahydrate ($MgCl_2{\cdot}6H_2O$) structure.

ACPD
15, 17797–17842, 2015

3.3 Deliquescence phase diagram of mixed NaCl–$MgCl_2$ particles

Figure 7 presents the measured first or second MDRHs ($MDRH_1$ or $MDRH_2$) and second DRHs of the NaCl–$MgCl_2$ mixture particles with different mole fractions along with the measured DRHs of the pure NaCl and $MgCl_2$ particles. As shown in Fig. 7, a clearly demarked phase diagram depicting their deliquescence behavior was obtained experimentally for the first time, for which, until now, there was no experimental data to the best of the authors' knowledge;

1. NaCl(s) + $MgCl_2$(s) phase: both NaCl and $MgCl_2$ are mixed as solids below the MDRHs at all mole fractions;
2. NaCl(s) + eutonic(aq) phase: a mixed phase of solid NaCl and aqueous eutonic components between the MDRHs and second DRHs for $X_{NaCl} > 0.026$;
3. NaCl(aq) + $MgCl_2$(aq) phase: both NaCl and $MgCl_2$ are mixed in the aqueous phase above the second DRHs at all mole fractions.

The second DRHs obtained experimentally agree well with the values calculated from the ionic activity products of the constituents predicted by the AIOMFAC model, as shown in Fig. 7 (dash-dotted curve for the second DRHs). On the other hand, the observed $MDRH_1$ (= 15.9 (±0.3) %) for most particles (of all mole fractions) was lower than the MDRH values of 36.1 % calculated from the AIOMFAC model and 32.0 % estimated using the bulk NaCl–$MgCl_2$–H_2O system phase diagram (Tang, 1976; Chan et al., 2000). This is similar to the case observed for the nebulized pure $MgCl_2$. On the other hand, particles with compositions of $X_{NaCl} = 0.1$ and 0.2 frequently show two MDRHs at 15.9 (±0.3) % ($MDRH_1$) and 33.0 (±0.5) % ($MDRH_2$). The dense ($0.1 \le X_{NaCl} \le 0.2$) and light ($0.01 \le X_{NaCl} \le 0.05$) brown shaded patterns in Fig. 7 indicate the high and low frequencies for encountering $MDRH_2$, respectively (Table 1). The eutonic composition ($X_{NaCl} = 0.026$), which was calculated theoretically from the AIOMFAC model, cannot be ascertained clearly from the experimental data as the deliquescence transition for these $MgCl_2$-dominant compositions (Fig. 4b and c) becomes

ACPD
15, 17797–17842, 2015

similar to that of the nebulized pure $MgCl_2$ (Fig. 1b). On the other hand, it should be close to the value of $X_{NaCl} = 0.029$ (NaCl =~ 1 % and $MgCl_2$ =~ 35 %) calculated from the phase diagram for the bulk NaCl–$MgCl_2$–H_2O system at 298.15 K based on equilibrium thermodynamics (Seidell and Linke, 1965; Tang, 1976). Chan et al. (2000) calculated a MDRH of 32.0 % and a second DRH of 70 % for an equimolar mixing ratio from the bulk NaCl –$MgCl_2$–H_2O system phase diagram (Seidell and Linke, 1965), but no experimental DRHs were reported.

All the mixed NaCl–$MgCl_2$ particles showed the first deliquescence transition at the $MDRH_1$ (= 15.9 (±0.3) %), regardless of the mixing ratio of the two salts, except for compositions of $0.01 \le X_{NaCl} \le 0.2$, particularly $X_{NaCl} = 0.1$ and 0.2, where Types B and C particles also exhibited a partial deliquescence transition at $MDRH_2$ (= 33.0 (±0.5) %) for the crystalline $MgCl_2{\cdot}6H_2O$-dominant eutonic components. Thermodynamically, as the first deliquescence transition of mixed-salts is governed by the water activity at the eutonic point, the MDRH of the mixed-salt particles is normally independent of the initial composition of the mixture. For the NaCl-rich particles of $X_{NaCl} > 0.026$, which contain more NaCl than the eutonic composition, as the NaCl mole fraction increases, the second DRH values approach the DRH of the pure NaCl salt. This suggests that for particles with $X_{NaCl} > 0.026$, the second-stage deliquescence is driven purely by the solid NaCl remaining after deliquescence of the eutonic composition (Li et al., 2014; Gupta et al., 2015).

3.4 Efflorescence phase diagram of mixed NaCl-$MgCl_2$ particles

Figure 8 shows the measured ERHs and MERHs for mixed NaCl–$MgCl_2$ particles with various mixing ratios as a function of the NaCl mole fraction. Similar to the deliquescence phase diagram, which showed three systematic phases, the efflorescence phase diagram is also composed of three distinct phases:

1. NaCl(aq) + $MgCl_2$(aq) phase: both NaCl and $MgCl_2$ are mixed in the aqueous phase above the first ERHs at all mixing ratios;

ACPD
15, 17797–17842, 2015

2. NaCl(s) + eutonic(aq) phase: a mixed phase of solid NaCl and aqueous eutonic components between the first ERH and second ERH (MERH) for $X_{NaCl} > 0.026$; and

3. NaCl(s) + $MgCl_2$(s) phase: both NaCl and $MgCl_2$ are mixed as solids below the second ERH (MERH) for $X_{NaCl} > 0.026$ and below the first ERHs for $X_{NaCl} \leq 0.026$.

This experimental phase diagram for efflorescence is reported for the first time, for which to the best of the authors' knowledge, there is neither a theoretical prediction nor experimental report. The first ERHs of NaCl-rich droplets ($X_{NaCl} > 0.026$) shift toward the pure NaCl limit (RH = 47.6– 45.7 %) with increasing NaCl mole fraction (see Fig. 8). This suggests that the first-stage efflorescence for particles of $X_{NaCl} > 0.026$ is driven purely by the homogeneous nucleation of NaCl, the rate of which increases with increasing NaCl mole fraction (Gupta et al., 2015). Chan et al. (2000) reported that the first ERH for the crystallization of pure NaCl is 38.0 % for an equimolar mixing ratio, which is within the range of the first ERH of 40.3–35.0 % (Figs. 4a and 8) measured for the same mixing ratio in the present work. Although they did not report MERH, MERHs were clearly observed in this study. For Types A and B particles, the measured $MERH_1$ were observed over a wide range (~ 10.4–2.9 %) because of the stochastic nucleation events leading to the crystallization of $MgCl_2{\cdot}4H_2O$ moieties. The $MERH_1$ range is similar to that for the nebulized pure $MgCl_2$ particles (ERH = 10.1–3.2 %). On the other hand, $MERH_2$ values for Type C particles of $X_{NaCl} = 0.1$ and 0.2 were in the ranges of ~ 15.2–11.9 % and ~ 23.7–15.3 %, which is just below their first ERHs of ~ 17.4–12.4 % and ~ 27.1–23.9 %, respectively, because the optimally-sized NaCl seeds, which are needed to facilitate heterogeneous nucleation leading to the crystallization of $MgCl_2{\cdot}6H_2O$, are available immediately after the first efflorescence transitions. The droplets with $MgCl_2$-dominant compositions, such as $X_{NaCl} = 0.026$ and 0.01, showed the single efflorescence transitions over an ERH range of 9.7–3.4 % and 6.2–4.0 %, respectively.

ACPD
15, 17797–17842, 2015

3.5 Spatial distribution of the effloresced $NaCl–MgCl_2$ solid particles

SEM/EDX was used to examine the morphology and spatial distribution of the chemical components in the effloresced $NaCl–MgCl_2$ solid particles at various mixing ratios after the humidifying and dehydration cycles. Figure 9a and b shows elemental X-ray mapping images for Na, Mg, O, and Na/Mg (mixed) and a secondary electron image (SEI) of NaCl-rich particles with $X_{NaCl} = 0.9$ (seawater-like mixing ratio) and $X_{NaCl} = 0.6$, respectively. The elemental X-ray maps in both cases suggest that Na (from NaCl) is concentrated in the central part, whereas Mg and O (from $MgCl_2{\cdot}4H_2O$) is more concentrated at the edges. This suggests that NaCl nucleates homogeneously to crystallize in the center at the first ERH, whereas the $MgCl_2{\cdot}4H_2O$-dominant eutonic phase solidifies on these central NaCl seeds at the second ERH (MERH), corroborating the efflorescence mechanism observed by OM. $MgCl_2$-rich or $MgCl_2$-dominant particles were not shown because $MgCl_2$ covers whole particles without a visible NaCl moiety and their hygroscopic behavior is similar to that of the nebulized pure $MgCl_2$ particles.

3.6 Atmospheric implications

Because Cl^- is the most abundant anion, and Na^+ and Mg^{2+} are the first and second most abundant cationic species, respectively, in nascent sea-salt (Seinfeld and Pandis, 2006), $NaCl–MgCl_2$ binary mixture particles can be good surrogates for the nascently generated inorganic-rich supermicron SSAs. For particles with an approximately seawater-like mixing ratio of $X_{NaCl} = 0.9$, the hygroscopic curve (2-D area ratio plots as a function of RH, as shown in Fig. 3) is similar to those obtained by OM for the particles nebulized from artificial seawater (Schindelholz et al., 2014) and by EDB measurements on sea-salt particles generated from filtered seawater (Tang et al., 1997). In addition, the hygroscopic curve for particles of $X_{NaCl} = 0.9$ is similar to that obtained for genuine ambient SSAs (Ahn et al., 2010), except that the real genuine SSAs, having other minor chemical species, such as Ca^{2+}, K^+, SO_4^{2-}, and organics, did not show distinct MDRH or MERH, as observed in this study for the case of $X_{NaCl} = 0.9$. On

ACPD
15, 17797–17842, 2015

the other hand, the hygroscopic behavior and growth curve in Fig. 3 deviated considerably from that of pure NaCl particles, as shown in Fig. 1a and by previous reports (Tang et al., 1997; Ahn et al., 2010; Schindelholz et al., 2014). These observations suggest that pure $MgCl_2$ species (Fig. 1b) play a strong role in the hygroscopicity of the NaCl–$MgCl_2$ mixture system as well as the nascent ambient SSAs.

Mg^{2+}, residing at the edges (core-shell type micro-structure, as shown in Fig. 9) and being in an aqueous phase even at very low RHs, i.e., at RHs higher than ~ 15.9 % and ~ 5 % in the humidifying (Fig. 7) and dehydration (Fig. 8) modes, respectively, has extremely important implications for nascent SSA heterogeneous chemistry (Wise et al., 2009; Woods et al., 2010, 2012; Liu et al., 2007). As NaCl–$MgCl_2$ binary mixture particles can maintain an aqueous phase over a much broader RH range than pure NaCl particles, they will be increasingly susceptible to reactions with gas phase inorganic and organic species, such as NO_x, SO_x, HNO_3/H_2SO_4, and dicarboxylic acids (DCAs). Liu et al. (2007) reported the faster uptake of gaseous HNO_3 into NaCl–$MgCl_2$ mixture particles with a seawater-like mixing ratio and ambient SSAs than into pure NaCl particles. The lack of knowledge, however, of the hygroscopic behavior and phases of NaCl–$MgCl_2$ mixture particles has resulted in large uncertainties for the determination of the uptake coefficient of HNO_3. Therefore, in terms of the aqueous phase chemistry of nascent SSAs, the hygroscopic behavior of NaCl–$MgCl_2$ mixture particles, systematically investigated in this study for the first time, is of higher relevance as nascent SSA surrogates than pure NaCl particles.

The NaCl moiety, crystallizing easily at higher RHs than $MgCl_2$, and the aqueous Mg^{2+} moiety, having a high surface tension and viscosity, may have a tendency to separate or fractionate in ambient SSAs. These chemical fractionations can occur even during wave breaking or bubble bursting processes on the sea surface (Keene et al., 2007). Therefore, fractionated NaCl-rich and $MgCl_2$-rich particles have often been reported for ambient SSAs (Wise et al., 2007; Ahn et al., 2010; Hara et al., 2014; Prather et al., 2013). $MgCl_2$-rich particles can maintain an aqueous phase over a much broader RH range during both humidifying and dehydration processes than NaCl-rich particles

ACPD
15, 17797–17842, 2015

(Figs. 7 and 8), suggesting that $MgCl_2$-rich particles will have a higher probability of reacting with gaseous species in the marine boundary layer (MBL). Both ambient and laboratory-generated SSAs show that organic species are mostly associated with Mg-rich inorganics (Keene et al., 2007; Prather et al., 2013). The unexpectedly low MDRH and MERH of $MgCl_2{\cdot}4H_2O$ moiety and the stochastic nature of heterogeneous nucleation for $MgCl_2{\cdot}6H_2O$ formation in the presence of optimally-sized seeds, together with the presence of organics, may partially explain the intriguing hygroscopic behavior of SSAs (Meskhidze et al., 2013). The heterogeneous crystallization of $MgCl_2{\cdot}6H_2O$ can also take place in the presence of other seeds in SSAs, such as easily crystallizing $CaSO_4$ (ERH = 80–90 %) (Xiao et al., 2008). Therefore, the hygroscopic study for all mixing ratios of the NaCl–$MgCl_2$ system covered in this study, including the $MgCl_2$-rich/dominant particles, can provide some insight into the physico-chemical characteristics and atmospheric chemistry of nascent SSAs.

4 Conclusions

The hygroscopic properties, physical states/phases, and chemical micro-structures of pure $MgCl_2$ particles and the two-component NaCl–$MgCl_2$ mixture particles deposited on substrates were studied by OM, in-situ RMS and SEM/EDX elemental X-ray mapping. The DRHs and ERHs of laboratory-generated aerosol particles of 1–10 µm size at room temperature were determined by monitoring the 2-D area change for particles on optical images with RH variations between ~ 3 and 90 %. During the humidifying process, wet-deposited particles from a $MgCl_2{\cdot}6H_2O$ solution showed a MDRH of 15.9 (±0.3) %. The characteristic –OH vibration signatures from in-situ RMS indicated the formation of $MgCl_2{\cdot}4H_2O$, rather than thermodynamically stable $MgCl_2{\cdot}6H_2O$, due to a kinetic barrier to nucleation and structural growth with limited condensed water during the dehydration process. The NaCl–$MgCl_2$ mixture particles with NaCl-rich compositions of $0.05 \leq X_{NaCl} \leq 0.9$ mostly showed two-stage deliquescence: first, with the dissolution of eutonic components, and second, with the complete dissolu-

ACPD
15, 17797–17842, 2015

tion of NaCl, typical for two component salt systems (Gupta et al., 2015; Li et al., 2014). The second DRH values approach the pure NaCl limit as the mole fraction of NaCl increases. Interestingly, NaCl-rich particles with composition of $X_{NaCl} = 0.1$ and 0.2 showed three different mutual deliquescence behaviors during the humidifying process, which was also confirmed by complementary in-situ RMS measurements. The first type showed an MDRH of 15.9 (±0.3) %; the second type showed a first MDRH at ∼ 15.9 (±0.3) %, an efflorescence-like transition to $MgCl_2{\cdot}6H_2O$ at RH in the range of ∼ 16.1–24.9 % and a second MDRH at ∼ 33.0 (±0.5) %; and the third type showed an MDRH at ∼ 33.0 (±0.5) %. These phenomena are rarely observed for NaCl-rich particles of $0.3 \leq X_{NaCl} \leq 0.9$ and also $X_{NaCl} = 0.05$, where most particles showed an MDRH at ∼ 15.9 (±0.3) %. Particles with $MgCl_2$-dominant compositions of $X_{NaCl} = 0.026$ (eutonic) and 0.01 mostly showed single-stage deliquescence behavior like pure $MgCl_2{\cdot}4H_2O$ particles with a DRH of 15.9 (±0.3) %.

During dehydration, NaCl–$MgCl_2$ mixture particles of $0.05 \leq X_{NaCl} \leq 0.9$ showed two-stage efflorescence: first, by the homogeneous nucleation of NaCl and second, by nucleation of the eutonic component at MERH, which is mostly independent of the aerosol compositions. The first ERH values approach the pure NaCl limit as the mole fraction of NaCl increases. $MgCl_2$-dominant particles with the eutonic composition ($X_{NaCl} = 0.026$) and $X_{NaCl} = 0.01$ showed single-stage efflorescence at ERHs ranging from 10.1 to 3.2 %. Most particles at all mixing ratios ($0.01 \leq X_{NaCl} \leq 0.9$) showed MERHs in the range, 10.4–2.9 %, forming $MgCl_2{\cdot}4H_2O$. On the other hand, a significant number of particles with $X_{NaCl} = 0.1$ and 0.2 were observed to undergo a second efflorescence at higher MERHs = 15.2–11.9 % and 23.7–15.3 %, respectively, to form $MgCl_2{\cdot}6H_2O$, which is coupled with the observation of the first MDRH at ∼ 33.0 % during the subsequent humidifying process. The observation of $MgCl_2{\cdot}6H_2O$ efflorescence at relatively higher RH ranges than $MgCl_2{\cdot}4H_2O$ efflorescence suggests that the presence of sufficient condensed water assists in hydrate-ion $[Mg(6H_2O)]^{2+}$ mobilization and that only optimally-sized crystalline NaCl can act as heterogeneous nucleation seeds to overcome the kinetic barrier, leading to the structural growth and crystalliza-

ACPD
15, 17797–17842, 2015

tion of $MgCl_2 \cdot 6H_2O$. SEM/EDX elemental X-ray mapping showed that the effloresced NaCl–$MgCl_2$ particles of NaCl-rich mixing ratios had the NaCl moiety homogeneously crystallized in the center, surrounded by $MgCl_2 \cdot 4H_2O$, forming a core-shell structure.

NaCl–$MgCl_2$ mixture aerosol particles can maintain an aqueous phase over a wider RH range than the pure NaCl particles, both in the humidifying and the dehydration modes, making their heterogeneous chemistry with atmospheric gas phase species more likely. The hygroscopic curves, Raman –OH vibrational signatures, phase diagrams obtained for DRHs and ERHs, and chemical X-ray maps of effloresced particles covering twelve mixing ratios ($0.01 \leq X_{NaCl} \leq 0.9$) provides a clear picture of the hygroscopic behavior and chemical micro-structure of NaCl–$MgCl_2$ mixture particles as nascent SSA surrogates. This can help characterize the mixing states, morphology, phases, and aqueous phase chemistry of ambient, nascent inorganic SSAs.

Author contributions. D. Gupta and H.-J. Eom contribute equally to this work.

Acknowledgements. This study was supported by Basic Science Research Programs through the National Research Foundation of Korea (NRF) funded by the Ministry of Education, Science, and Technology (NRF-2012R1A2A1A05026329).

References

Ahn, K.-H., Kim, S.-M., Jung, H.-J., Lee, M.-J., Eom, H.-J., Maskey, S., and Ro, C.-U.: Combined use of optical and electron microscopic techniques for the measurement of hygroscopic property, chemical composition, and morphology of individual aerosol particles, Anal. Chem., 82, 7999–8009, doi:10.1021/ac101432y, 2010.

Ansari, A. S. and Pandis, S. N.: Prediction of multicomponent inorganic atmospheric aerosol behavior, Atmos. Environ., 33, 745–757, doi:10.1016/S1352-2310(98)00221-0, 1999.

Callahan, K. M., Casillas-Ituarte, N. N., Roeselovaì, M., Allen, H. C., and Tobias, D. J.: Solvation of magnesium dication: molecular dynamics simulation and vibrational spectroscopic study of magnesium chloride in aqueous solutions, J. Phys. Chem. A, 114, 5141–5148, doi:10.1021/jp909132a, 2010.

ACPD
15, 17797–17842, 2015

Carslaw, K. S., Clegg, S. L., and Brimblecombe, P.: A Thermodynamic Model of the System HCl-HNO_3-H_2SO_4-H_2O, Including Solubilities of HBr, from <200 to 328 K, J. Phys. Chem., 99, 11557–11574, doi:10.1021/j100029a039, 1995.

Casillas-Ituarte, N. N., Callahan, K. M., Tang, C. Y., Chen, X., Roeselová, M., Tobias, D. J., and Allen, H. C.: Surface organization of aqueous $MgCl_2$ and application to atmospheric marine aerosol chemistry, P. Natl. Acad. Sci. USA, 107, 6616–6621, doi:10.1073/pnas.0912322107, 2010.

Chan, C. K., Ha, Z., and Choi, M. Y.: Study of water activities of aerosols of mixtures of sodium and magnesium salts, Atmos. Environ., 34, 4795–4803, doi:10.1016/S1352-2310(00)00252-1, 2000.

Clegg, S. L., Brimblecombe, P., and Wexler, A. S.: Thermodynamic model of the system H^+-NH_4^+-SO_4^{2-}-NO_3^--H_2O at tropospheric temperatures, J. Phys. Chem. A, 102, 2137–2154, doi:10.1021/jp973042r, 1998a.

Clegg, S. L., Brimblecombe, P., and Wexler, A. S.: Thermodynamic model of the system H^+-NH_4^+-Na^+-SO_4^{2-}-NO_3^--Cl^--H_2O at 298.15 K, J. Phys. Chem. A, 102, 2155–2171, doi:10.1021/jp973043j, 1998b.

Cohen, M. D., Flagan, R. C., and Seinfeld, J. H.: Studies of concentrated electrolyte solutions using the electrodynamic balance. 3. Solute nucleation, J. Phys. Chem., 91, 4583–4590, doi:10.1021/j100301a031, 1987.

Cziczo, D. J. and Abbatt, J. P. D.: Infrared observations of the response of NaCl, $MgCl_2$, NH_4HSO_4, and NH_4NO_3 aerosols to changes in relative humidity from 298 to 238 K, J. Phys. Chem. A, 104, 2038–2047, doi:10.1021/jp9931408, 2000.

Cziczo, D. J., Nowak, J. B., Hu, J. H., and Abbatt, J. P. D.: Infrared spectroscopy of model tropospheric aerosols as a function of relative humidity: observation of deliquescence and crystallization, J. Geophys. Res.-Atmos., 102, 18843–18850, doi:10.1029/97jd01361, 1997.

Drozd, G., Woo, J., Häkkinen, S. A. K., Nenes, A., and McNeill, V. F.: Inorganic salts interact with oxalic acid in submicron particles to form material with low hygroscopicity and volatility, Atmos. Chem. Phys., 14, 5205–5215, doi:10.5194/acp-14-5205-2014, 2014.

Eom, H.-J., Gupta, D., Li, X., Jung, H.-J., Kim, H., and Ro, C.-U.: Influence of collecting substrates on the characterization of hygroscopic properties of inorganic aerosol particles, Anal. Chem., 86, 2648–2656, doi:10.1021/ac4042075, 2014.

Finlayson-Pitts, B. J. and Pitts, J. N.: Chemistry of the Upper and Lower Atmosphere: Theory, Experiments, and Applications, Academic Press, San Diego, XXII, 969 pp., 2000.

ACPD
15, 17797–17842, 2015

Ge, Z., Wexler, A. S., and Johnston, M. V.: Multicomponent aerosol crystallization, J. Colloid Interface Sci., 183, 68–77, doi:10.1006/jcis.1996.0519, 1996.
Ghorai, S., Wang, B., Tivanski, A., and Laskin, A.: Hygroscopic Properties of Internally Mixed Particles Composed of NaCl and Water-Soluble Organic Acids, Environ. Sci. Technol., 48, 2234–2241, doi:10.1021/es404727u, 2014.
Gough, R. V., Chevrier, V. F., and Tolbert, M. A.: Formation of aqueous solutions on Mars via deliquescence of chloride–perchlorate binary mixtures, Earth Planet. Sc. Lett., 393, 73–82, doi:10.1016/j.epsl.2014.02.002, 2014.
Gupta, D., Kim, H., Park, G., Li, X., Eom, H.-J., and Ro, C.-U.: Hygroscopic properties of NaCl and $NaNO_3$ mixture particles as reacted inorganic sea-salt aerosol surrogates, Atmos. Chem. Phys., 15, 3379–3393, doi:10.5194/acp-15-3379-2015, 2015.
Ha, Z. and Chan, C. K.: The water activities of $MgCl_2$, $Mg(NO_3)_2$, $MgSO_4$, and their mixtures, Aerosol Sci. Tech., 31, 154–169, doi:10.1080/027868299304219, 1999.
Hara, K., Osada, K., Yabuki, M., and Yamanouchi, T.: Seasonal variation of fractionated sea-salt particles on the Antarctic coast, Geophys. Res. Lett., 39, L18801, doi:10.1029/2012gl052761, 2012.
Hara, K., Nakazawa, F., Fujita, S., Fukui, K., Enomoto, H., and Sugiyama, S.: Horizontal distributions of aerosol constituents and their mixing states in Antarctica during the JASE traverse, Atmos. Chem. Phys., 14, 10211–10230, doi:10.5194/acp-14-10211-2014, 2014.
Haywood, J. and Boucher, O.: Estimates of the direct and indirect radiative forcing due to tropospheric aerosols: a review, Rev. Geophys., 38, 513–543, doi:10.1029/1999rg000078, 2000.
Hennings, E., Schmidt, H., and Voigt, W.: Crystal structures of hydrates of simple inorganic salts. I. Water-rich magnesium halide hydrates $MgCl_2{\cdot}8H_2O$, $MgCl_2{\cdot}12H_2O$, $MgBr_2{\cdot}6H_2O$, $MgBr_2{\cdot}9H_2O$, $MgI_2{\cdot}8H_2O$ and $MgI_2{\cdot}9H_2O$, Acta Cryst. C, 69, 1292–1300, doi:10.1107/s0108270113028138, 2013.
Keene, W. C., Maring, H., Maben, J. R., Kieber, D. J., Pszenny, A. A. P., Dahl, E. E., Izaguirre, M. A., Davis, A. J., Long, M. S., Zhou, X., Smoydzin, L., and Sander, R.: Chemical and physical characteristics of nascent aerosols produced by bursting bubbles at a model air–sea interface, J. Geophys. Res.-Atmos., 112, D21202, doi:10.1029/2007jd008464, 2007.
Kelly, J. T. and Wexler, A. S.: Thermodynamics of carbonates and hydrates related to heterogeneous reactions involving mineral aerosol, J. Geophys. Res.-Atmos., 110, D11201, doi:10.1029/2004jd005583, 2005.

ACPD
15, 17797–17842, 2015

King, S. M., Butcher, A. C., Rosenoern, T., Coz, E., Lieke, K. I., de Leeuw, G., Nilsson, E. D., and Bilde, M.: Investigating primary marine aerosol properties: CCN activity of sea salt and mixed inorganic–organic particles, Environ. Sci. Technol., 46, 10405–10412, doi:10.1021/es300574u, 2012.

Krieger, U. K., Marcolli, C., and Reid, J. P.: Exploring the complexity of aerosol particle properties and processes using single particle techniques, Chem. Soc. Rev., 41, 6631–6662, doi:10.1039/c2cs35082c, 2012.

Krueger, B. J., Grassian, V. H., Iedema, M. J., Cowin, J. P., and Laskin, A.: Probing Heterogeneous Chemistry of Individual Atmospheric Particles Using Scanning Electron Microscopy and Energy-Dispersive X-ray Analysis, Anal. Chem., 75, 5170–5179, doi:10.1021/ac034455t, 2003.

Li, X., Gupta, D., Eom, H.-J., Kim, H., and Ro, C.-U.: Deliquescence and efflorescence behavior of individual NaCl and KCl mixture aerosol particles, Atmos. Environ., 82, 36–43, doi:10.1016/j.atmosenv.2013.10.011, 2014.

Lide, D. R.: Handbook of Chemistry and Physics, 83rd edn., CRC Press, Boca Raton, Florida, 2002.

Liu, Y., Cain, J. P., Wang, H., and Laskin, A.: Kinetic study of heterogeneous reaction of deliquesced NaCl particles with gaseous HNO_3 using particle-on-substrate stagnation flow reactor approach, J. Phys. Chem. A, 111, 10026–10043, doi:10.1021/jp072005p, 2007.

Ma, Q., Ma, J., Liu, C., Lai, C., and He, H.: Laboratory study on the hygroscopic behavior of external and internal C2–C4 dicarboxylic acid–NaCl mixtures, Environ. Sci. Technol., 47, 10381–10388, doi:10.1021/es4023267, 2013.

Martin, S. T.: Phase transitions of aqueous atmospheric particles, Chem. Rev., 100, 3403–3454, doi:10.1021/cr990034t, 2000.

Meskhidze, N., Petters, M. D., Tsigaridis, K., Bates, T., O'Dowd, C., Reid, J., Lewis, E. R., Gantt, B., Anguelova, M. D., Bhave, P. V., Bird, J., Callaghan, A. H., Ceburnis, D., Chang, R., Clarke, A., de Leeuw, G., Deane, G., DeMott, P. J., Elliot, S., Facchini, M. C., Fairall, C. W., Hawkins, L., Hu, Y., Hudson, J. G., Johnson, M. S., Kaku, K. C., Keene, W. C., Kieber, D. J., Long, M. S., Mårtensson, M., Modini, R. L., Osburn, C. L., Prather, K. A., Pszenny, A., Rinaldi, M., Russell, L. M., Salter, M., Sayer, A. M., Smirnov, A., Suda, S. R., Toth, T. D., Worsnop, D. R., Wozniak, A., and Zorn, S. R.: Production mechanisms, number concentration, size distribution, chemical composition, and optical properties of sea spray aerosols, Atmos. Sci. Lett., 14, 207–213, doi:10.1002/asl2.441, 2013.

ACPD
15, 17797–17842, 2015

Mikhailov, E., Vlasenko, S., Niessner, R., and Pöschl, U.: Interaction of aerosol particles composed of protein and saltswith water vapor: hygroscopic growth and microstructural rearrangement, Atmos. Chem. Phys., 4, 323–350, doi:10.5194/acp-4-323-2004, 2004.

Mikhailov, E., Vlasenko, S., Martin, S. T., Koop, T., and Pöschl, U.: Amorphous and crystalline aerosol particles interacting with water vapor: conceptual framework and experimental evidence for restructuring, phase transitions and kinetic limitations, Atmos. Chem. Phys., 9, 9491–9522, doi:10.5194/acp-9-9491-2009, 2009.

Musick, J., Popp, J., and Kiefer, W.: Raman spectroscopic and elastic light scattering investigations of chemical reactions in single electrodynamically levitated microparticles, J. Mol. Struct., 480–481, 317–321, doi:10.1016/S0022-2860(98)00705-4, 1999.

Niedermeier, D., Wex, H., Voigtländer, J., Stratmann, F., Brüggemann, E., Kiselev, A., Henk, H., and Heintzenberg, J.: LACIS-measurements and parameterization of sea-salt particle hygroscopic growth and activation, Atmos. Chem. Phys., 8, 579–590, doi:10.5194/acp-8-579-2008, 2008.

Park, K., Kim, J.-S., and Miller, A.: A study on effects of size and structure on hygroscopicity of nanoparticles using a tandem differential mobility analyzer and TEM, J. Nanopart. Res., 11, 175–183, doi:10.1007/s11051-008-9462-4, 2009.

Pöhlker, C., Saturno, J., Krüger, M. L., Förster, J.-D., Weigand, M., Wiedemann, K. T., Bechtel, M., Artaxo, P., and Andreae, M. O.: Efflorescence upon humidification? X-ray microspectroscopic in situ observation of changes in aerosol microstructure and phase state upon hydration, Geophys. Res. Lett., 41, 2014GL059409, doi:10.1002/2014gl059409, 2014.

Prather, K. A., Bertram, T. H., Grassian, V. H., Deane, G. B., Stokes, M. D., DeMott, P. J., Aluwihare, L. I., Palenik, B. P., Azam, F., Seinfeld, J. H., Moffet, R. C., Molina, M. J., Cappa, C. D., Geiger, F. M., Roberts, G. C., Russell, L. M., Ault, A. P., Baltrusaitis, J., Collins, D. B., Corrigan, C. E., Cuadra-Rodriguez, L. A., Ebben, C. J., Forestieri, S. D., Guasco, T. L., Hersey, S. P., Kim, M. J., Lambert, W. F., Modini, R. L., Mui, W., Pedler, B. E., Ruppel, M. J., Ryder, O. S., Schoepp, N. G., Sullivan, R. C., and Zhao, D.: Bringing the ocean into the laboratory to probe the chemical complexity of sea spray aerosol, P. Natl. Acad. Sci. USA, 110, 7550–7555, doi:10.1073/pnas.1300262110, 2013.

Saul, T. D., Tolocka, M. P., and Johnston, M. V.: Reactive Uptake of Nitric Acid onto Sodium Chloride Aerosols Across a Wide Range of Relative Humidities, J. Phys. Chem. A, 110, 7614–7620, doi:10.1021/jp060639a, 2006.

ACPD
15, 17797–17842, 2015

Schindelholz, E., Risteen, B. E., and Kelly, R. G.: Effect of relative humidity on corrosion of steel under sea salt aerosol proxies: II. $MgCl_2$, artificial seawater, J. Electrochem. Soc., 161, C460–C470, doi:10.1149/2.0231410jes, 2014.

Schlenker, J. C. and Martin, S. T.: Crystallization pathways of sulfate-nitrate-ammonium aerosol particles, J. Phys. Chem. A, 109, 9980–9985, doi:10.1021/jp052973x, 2005.

Seidell, A. and Linke, W. F.: Solubilities of Inorganic and Metal Organic Compounds, 4th edn., American Chemical Society, Washington, DC, 1965.

Seinfeld, J. H. and Pandis, S. N.: Atmospheric Chemistry and Physics: From Air Pollution to Climate Change, 2nd edn., J. Wiley & Sons Inc., Hoboken, NJ, 2006.

Tang, I. N.: Phase transformation and growth of aerosol particles composed of mixed salts, J. Aerosol Sci., 7, 361–371, doi:10.1016/0021-8502(76)90022-7, 1976.

Tang, I. N., Tridico, A. C., and Fung, K. H.: Thermodynamic and optical properties of sea salt aerosols, J. Geophys. Res.-Atmos., 102, 23269–23275, doi:10.1029/97jd01806, 1997.

ten Brink, H. M.: Reactive uptake of HNO_3 and H_2SO_4 in sea-salt (NaCl) particles, J. Aerosol Sci., 29, 57–64, doi:10.1016/S0021-8502(97)00460-6, 1998.

Wang, P., Pitzer, K. S., and Simonson, J. M.: Thermodynamic properties of aqueous magnesium chloride solutions from 250 to 600 K and to 100 MPa, J. Phys. Chem. Ref. Data., 27, 971–991, doi:10.1063/1.556026, 1998.

Wexler, A. S. and Clegg, S. L.: Atmospheric aerosol models for systems including the ions H^+, NH_4^+, Na^+, SO_4^{2-}, NO_3^-, Cl^-, Br^-, and H_2O, J. Geophys. Res.-Atmos., 107, ACH 14-11–ACH 14-14, doi:10.1029/2001jd000451, 2002.

Wexler, A. S. and Seinfeld, J. H.: Second-generation inorganic aerosol model, Atmos. Environ., 27A, 25, 2731–2748, doi:10.1016/0960-1686(91)90203-J, 1991.

Wise, M. E., Semeniuk, T. A., Bruintjes, R., Martin, S. T., Russell, L. M., and Buseck, P. R.: Hygroscopic behavior of NaCl-bearing natural aerosol particles using environmental transmission electron microscopy, J. Geophys. Res.-Atmos., 112, D10224, doi:10.1029/2006jd007678, 2007.

Wise, M. E., Freney, E. J., Tyree, C. A., Allen, J. O., Martin, S. T., Russell, L. M., and Buseck, P. R.: Hygroscopic behavior and liquid-layer composition of aerosol particles generated from natural and artificial seawater, J. Geophys. Res.-Atmos., 114, D03201, doi:10.1029/2008jd010449, 2009.

ACPD
15, 17797–17842, 2015

Woods, E., Chung, D., Lanney, H. M., and Ashwell, B. A.: Surface morphology and phase transitions in mixed NaCl/$MgSO_4$ aerosol particles, J. Phys. Chem. A, 114, 2837–2844, doi:10.1021/jp911133j, 2010.

Woods, E., Yi, C., Gerson, J. R., and Zaman, R. A.: Uptake of pyrene by NaCl, $NaNO_3$, and $MgCl_2$ aerosol particles, J. Phys. Chem. A, 116, 4137–4143, doi:10.1021/jp3014145, 2012.

Xiao, H.-S., Dong, J.-L., Wang, L.-Y., Zhao, L.-J., Wang, F., and Zhang, Y.-H.: Spatially resolved micro-Raman observation on the phase separation of effloresced sea salt droplets, Environ. Sci. Technol., 42, 8698–8702, doi:10.1021/es801181f, 2008.

Zuend, A., Marcolli, C., Luo, B. P., and Peter, T.: A thermodynamic model of mixed organic–inorganic aerosols to predict activity coefficients, Atmos. Chem. Phys., 8, 4559–4593, doi:10.5194/acp-8-4559-2008, 2008.

Zuend, A., Marcolli, C., Booth, A. M., Lienhard, D. M., Soonsin, V., Krieger, U. K., Topping, D. O., McFiggans, G., Peter, T., and Seinfeld, J. H.: New and extended parameterization of the thermodynamic model AIOMFAC: calculation of activity coefficients for organic–inorganic mixtures containing carboxyl, hydroxyl, carbonyl, ether, ester, alkenyl, alkyl, and aromatic functional groups, Atmos. Chem. Phys., 11, 9155–9206, doi:10.5194/acp-11-9155-2011, 2011.

ACPD
15, 17797–17842, 2015

Table 1. Encountering frequencies (in %) of Types A, B, and C particles, showing different mutual deliquescence behavior (details in text), at various mixing ratios of NaCl–$MgCl_2$.

Mole fraction of NaCl (X_{NaCl})	Encountering frequencies (in %)		
	Type A particles	Type B particles	Type C particles
0.01	94	6	–
0.026	94	6	–
0.05	96	4	–
0.1	24	29	47
0.2	36	45	18
$0.3 \leq X_{NaCl} \leq 0.9$	100	–	–

ACPD
15, 17797–17842, 2015

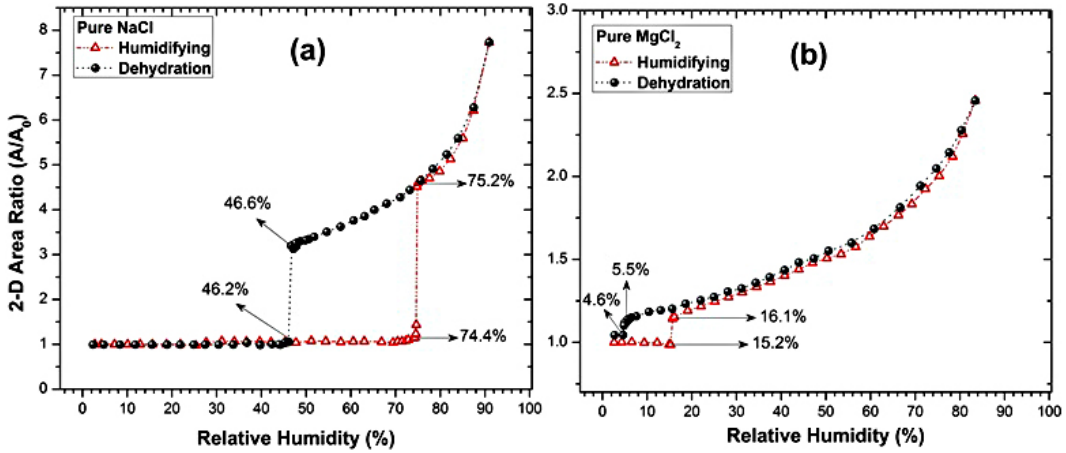

Figure 1. Plot of 2-D area ratio (A/A_0) of nebulized pure **(a)** NaCl and **(b)** $MgCl_2$ as a function of the RH. The recorded transition RHs in both humidifying and dehydration processes are marked with arrows.

ACPD
15, 17797–17842, 2015

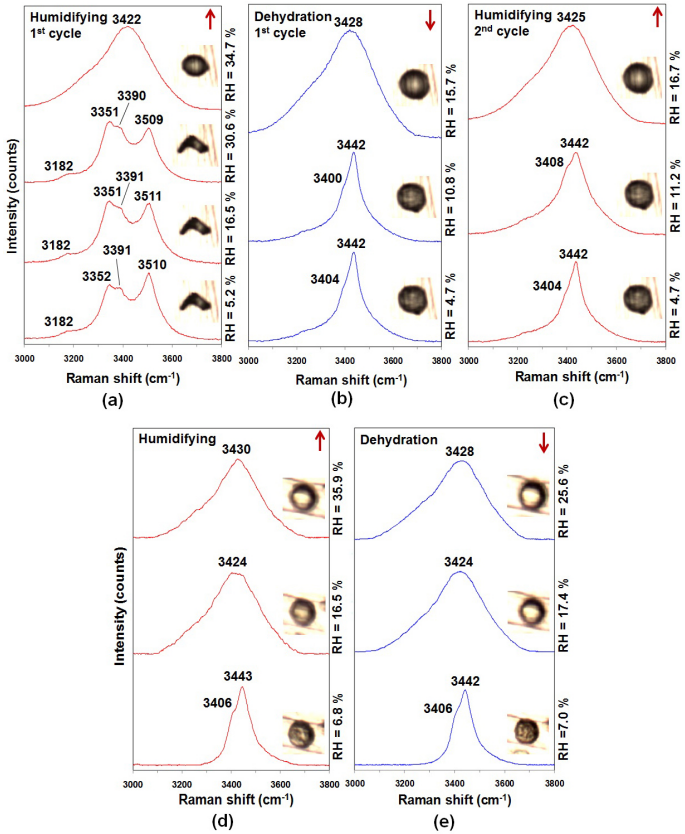

Figure 2. Optical images and corresponding Raman spectra obtained by in-situ RMS, for a representative dry-deposited $MgCl_2{\cdot}6H_2O$ particle during **(a)** humidifying (1st cycle), **(b)** dehydration (1st cycle), and **(c)** humidifying (2nd cycle) processes and for a representative wet-deposited $MgCl_2$ particle during **(d)** humidifying and **(e)** dehydration processes.

ACPD
15, 17797–17842, 2015

Hygroscopic behavior of $NaCl–MgCl_2$ mixture particles

D. Gupta et al.

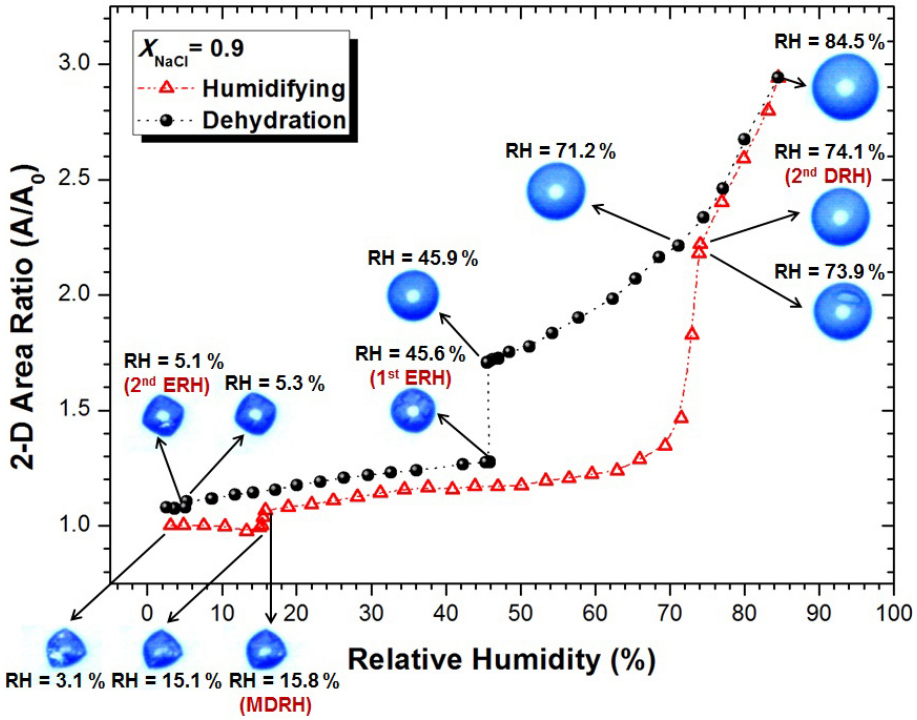

Figure 3. Plot of 2-D area ratio (A/A_0) of a NaCl-rich particle with a seawater-like mixing ratio of X_{NaCl} = 0.9 as a function of RH. The recorded optical images of the particle/droplet along with transition RHs in both humidifying and dehydration processes are marked with arrows.

ACPD
15, 17797–17842, 2015

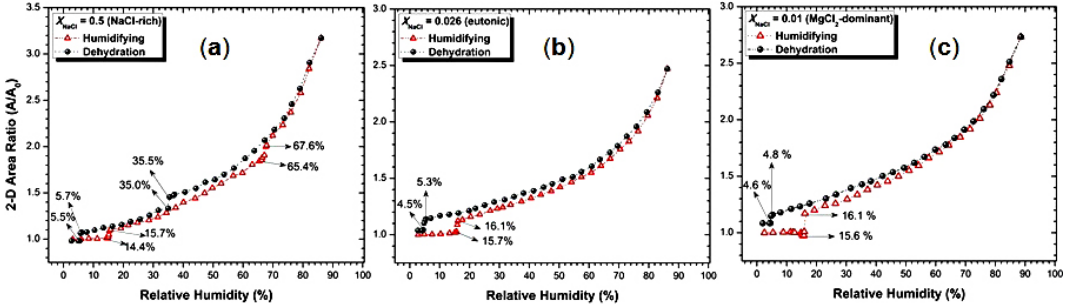

Figure 4. Plots of 2-D area ratio (A/A_0) of NaCl–$MgCl_2$ mixture aerosol particles with **(a)** NaCl-rich mixing ratio of $X_{NaCl} = 0.5$; **(b)** $MgCl_2$-dominant eutonic composition of $X_{NaCl} = 0.026$; and **(c)** $MgCl_2$-dominant mixing ratio of $X_{NaCl} = 0.01$ as a function of RH. The recorded transition relative humidities in both humidifying and dehydration processes are marked with arrows.

ACPD
15, 17797–17842, 2015

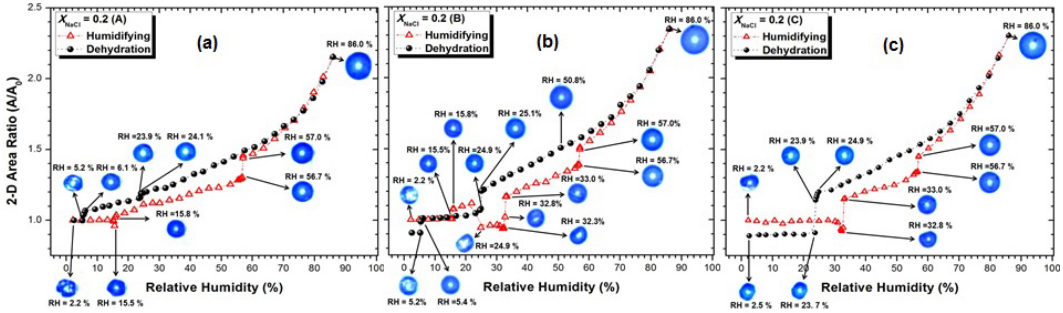

Figure 5. Plots of the 2-D area ratio (A/A_0) of three representative particles with a composition of X_{NaCl} = 0.2, showing different deliquescence behaviors during the humidifying process, as a function of RH. During the humidifying process, **(a)** "Type A" particle shows two deliquescence transitions with MDRH of 15.8 %, **(b)** "Type B" particle shows three deliquescence transitions as well as one efflorescence transition, and **(c)** "Type C" particle shows two deliquescence transitions with MDRH of 33.0 %. During the dehydration process, Types A and B particles show the second ERH of 5.2 %, whereas the Type C particle shows a second ERH of 23.7 %. The recorded optical images of the particles/droplets along with the transition RHs during both humidifying and dehydration processes are marked with arrows.

ACPD
15, 17797–17842, 2015

Hygroscopic behavior of NaCl–$MgCl_2$ mixture particles

D. Gupta et al.

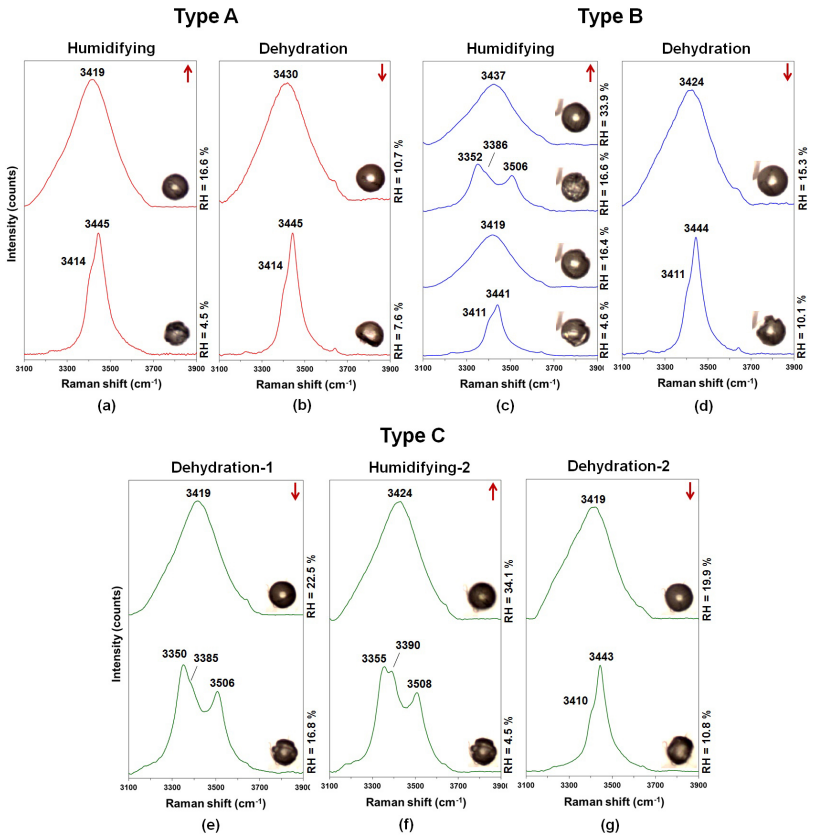

Figure 6. Characteristic OH-stretching Raman spectra and corresponding optical images of $NaCl–MgCl_2$ mixture particles with a composition of $X_{NaCl} = 0.2$, recorded by in-situ RMS. Three types of particles showing different hygroscopic behavior are shown. See the text for a detailed explanation.

ACPD
15, 17797–17842, 2015

Hygroscopic behavior of $NaCl–MgCl_2$ mixture particles

D. Gupta et al.

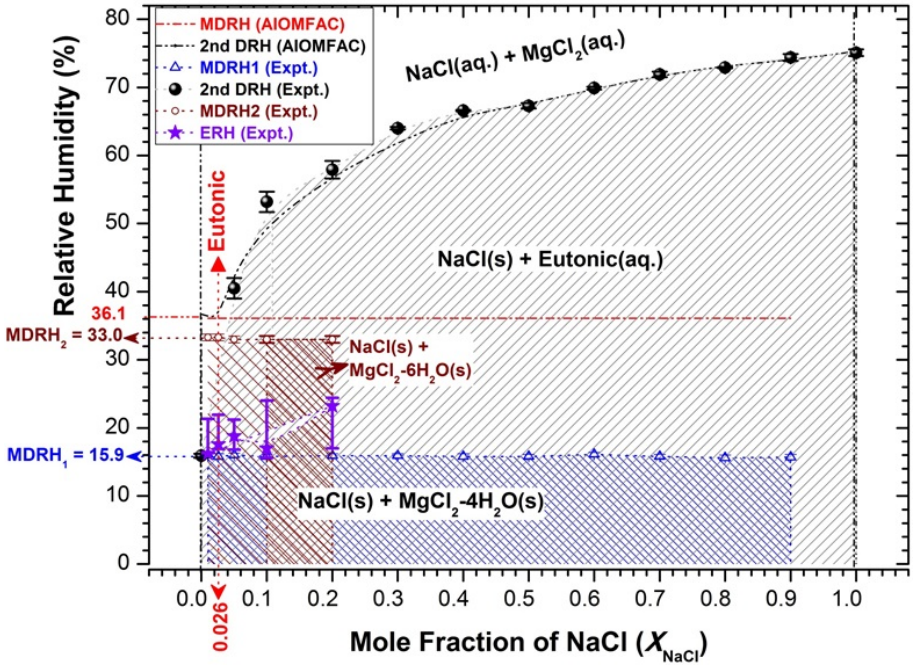

Figure 7. Measured MDRHs ($MDRH_1 = 15.9\,(\pm 0.5)\,\%$ ⇒ open blue triangles; $MDRH_2 = 33.0\,(\pm 0.5)\,\%$ ⇒ open brown circles) and the second DRH (closed black circles) and calculated MDRH (dotted red line) and the second DRHs (dash-dotted black curve) from the AIOMFAC, plotted as a function of the mole fraction of NaCl in NaCl–$MgCl_2$ mixture particles. The phase notations shown in brackets are: s = solid; and aq = aqueous. The brown shaded portion is where particles with three types of transitions (Types A, B, and C as in text) were observed for $X_{NaCl} = 0.1$ and 0.2. The dense and light brown shaded patterns indicate the high and low encountering frequencies of Types B and C particles, respectively. The average and range of ERHs observed during the humidifying process for Type B particles are represented by purple stars and bars, respectively.

ACPD
15, 17797–17842, 2015

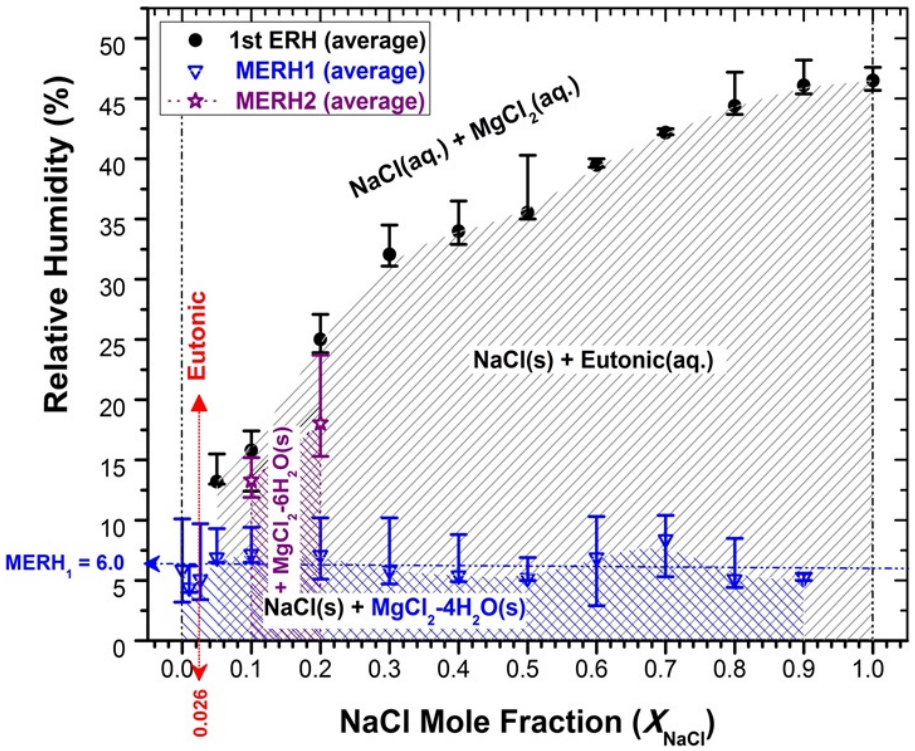

Figure 8. Measured first ERH values (closed black circles) and second ERH values (open blue triangles ($MERH_1$ for $MgCl_2{\cdot}4H_2O$ crystallization in Types A or B particles) and open purple stars ($MERH_2$ for $MgCl_2{\cdot}6H_2O$ crystallization in Type C particles)) as a function of the mole fraction of NaCl in NaCl–$MgCl_2$ mixture particles. The phase notations shown in brackets are s = solid; and aq = aqueous.

ACPD
15, 17797–17842, 2015

Hygroscopic behavior of NaCl–$MgCl_2$ mixture particles

D. Gupta et al.

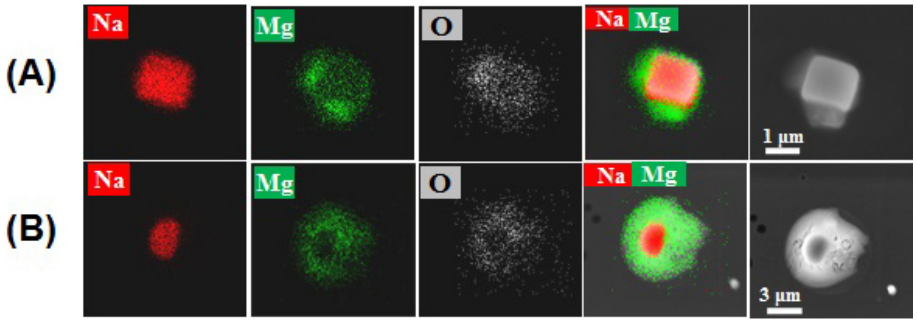

Figure 9. Elemental X-ray maps for Na (from NaCl), Mg (from $MgCl_2$), O (from $MgCl_2 \cdot xH_2O$), and mixed Na/Mg and secondary electron images (SEIs) of the effloresced NaCl–$MgCl_2$ mixture particles with compositions of **(a)** $X_{NaCl} = 0.9$ (NaCl-rich, seawater-like mixing ratio) and **(b)** $X_{NaCl} = 0.6$.

ACPD
15, 17797–17842, 2015